Integration of Droplet Microfluidics with a Nanopore Sensor

Enas Osman

Thesis submitted to the Faculty of Graduate and Postdoctoral Studies

in partial fulfillment of the requirements for

Master of Applied Science – Biomedical Engineering

Faculty of Engineering

University of Ottawa

Abstract

The integration of droplet microfluidics devices with nanopore sensors offers a powerful and miniaturized sensing platform. Such devices can utilize the pre-processing capabilities of microfluidics in conjunction with single molecule sensing offered by nanopores. Microfluidics devices utilizing segmented flow (droplets) allow the compartmentalization of chemical and biological reagents in droplets reducing the processing time and associated cost, which is advantageous to biomolecular applications. Droplet microfluidics have been used in diagnostics and therapeutic applications such as cell and biomarker detection, gene amplification, and drug delivery.

Nanopore sensors are currently used in investigating DNA and gene detection, protein-protein interactions, protein folding, and enzymatic kinetic reactions.

This thesis proposes a design and outlines a methodology to integrate nanopore sensors within a droplet microfluidic device. The chapters are organized in highlighting three main objectives. The first objective is creating the segmented flow of oil-KCl droplets using a T-junction microfluidic design. The second objective is measuring the conductance of the segmented flow prior to the nanopore integration by using two side channel-AgCl electrodes. Subsequently, the third objective is integrating the droplet microfluidic device with a silicon nitride chip for nanopore fabrication. The nanopore is then created using controlled dielectric breakdown (CBD) method for DNA detection within droplets.

The results show the feasibility of sensing individual DNA molecules within droplets using a nanopore sensor. The implemented approach expands upon nanopore applications to detect different samples simultaneously, fast food-borne pathogens and tumor discrimination in cancer biology. We anticipate that this integration is the future of nanopore sensors.

Statement of Originality

The content presented in this document is the product of original work performed by the author at the University of Ottawa under the supervision of Professor Michel Godin.

In partial fulfillment of the requirements for the degree of Master of Science (Engineering) at the University of Ottawa, this work was presented at the Ottawa Carleton Institute for Biomedical Engineering Seminar Series:

Enas Osman and Michel Godin, Integration of droplet microfluidics with a Nanopore Sensor. Ottawa Carleton Institute for Biomedical Engineering, March 20th, 2018.

Posters on the same topic were also presented at the 10th Annual Graduation Student Competition, Mar 27th, 2018 (uOttawa) and MDII & CREATE-BEST Poster Day, September 25th, 2018 (uOttawa).

Statement of contribution

The entirety of this document was written by the author. All figures and tables were created by the author unless otherwise mentioned in the caption. The work presented were performed by the author including, photomask designs, fabrication of devices (photolithography, wet etching, PDMS mold replication), testing of devices, segmented flow conductance measurement, nanopore sensing experiments, and data collection. The electrical setup for conductance measurement with the Labview® code for data viewing and recording used in Chapter 3 were created with the help of Professor Michel Godin. The T-junction devices mentioned in Chapter 2 (figure 8) and Chapter 3 (Figure 11A, B) was designed by Dr. Radin Tahvildari. The nanopore fabrication, open pore conductance viewing and PSD measurement Labview® codes were created by the Tabard-Cossa lab.

Acknowledgments

I would like to thank my supervisor Prof. Michel Godin for his constant encouragement and enthusiasm about the project. I am very grateful for his style of guiding and his joyful spirit. I consider myself very lucky for getting the opportunity to work with Prof. Godin and be part of his team. Although, this has been very challenging, it has given me the greatest gratification.

I would also like to thank Dr. Ali Sohi for his patience and selfless teachings in the beginning of my work and throughout the journey. He has set a good foundation for me to build on. I thoroughly enjoyed our morning discussions about work and life in general. Additionally, I want to thank Eric Beamish for being the nanopore expert, he has been a great colleague and a friend. I can confidently say that all the members in the lab are one of the greatest people I have ever got the pleasure to work with.

I would also like to extend my gratitude to Dr. Ainara Benavente-Babace, Rushi Panchal, Karan Dhingra, Adefemi Adeyemi, and Radin Tahvildari for being great friends and colleagues, without their help and moral support, this journey would have been extremely difficult.

Finally, this would not have been possible without my family and friends, my parents Azhari Osman and Sadiaa Yousif for their constant encouragement and support. I am very fortunate to have such wonderful and caring parents. Special thanks to my father for his financial support throughout my studies and for doing everything he could to be there and support us in every way. I would also like to thank my brothers Hisham and Mohammed, my amazing sisters and best friends Fatima and Alla for listening to me complaining for two years and for always believing in me.

إلى أمي الحبيبة:

أقدم لك بالغ الشكر والتقدير على مجهودك وسهرك ودعائك المستمر لي ولإخوتي. أشكرك على صبرك ورعايتك لنا طول هذه السنين ومهما حاولت، لن أستطير أن رد الجميل. أود أن أهدي لك أطروحة الماجستير هذه لاستمرارك في إضاءة طريق النجاح والتفوق لي طوال هذه الأعوام.

أخيراً أدعو الله أن يطيل في عمر والدي ويرزقهما السعادة في الدنيا والآخرة.

List of Abbreviations

General

- CBD: Controlled breakdown
- DAQ: Data acquisition card
- mV: Millivolt
- nA: Nanoampere
- pA: Picoampere
- PCR: Polymerase chain reaction
- ddPCR: Droplet digital polymerase chain reaction
- LAMP: Loop-mediated isothermal amplification
- PSD: Power spectral density
- PTFE: Polytetrafluoroethylene
- SNR: Signal-to-noise ratio
- TEM: Transmission electron microscopy
- DMN: Droplet microfluidic-nanopore
- BNC: Bayonet Neill - Concelman Connector
- UV: Ultraviolet

Chemical

- Ag: Silver
- AgCl: Silver chloride
- bp: Base pair
- DNA: Deoxyribonucleic acid
- ssDNA: Single-stranded DNA

- dsDNA: Double-stranded DNA
- KCl: Potassium chloride
- LiCl: Lithium chloride
- SDS: Sodium dodecyl sulphate
- PDMS: Polydimethylsiloxane
- PEEK: Polyether ether ketone
- RNA: Ribonucleic acid
- Si: Silicon
- SiN: Silicon nitride

Table of Contents

List of Figures

List of Tables

Chapter 1 Introduction

The development of novel biological sensing platforms can have major impacts in many disciplines including analytical biochemistry, biophysics, medicine and biomedical engineering [1]. Research into the development of new sensing platforms aims to increase sensitivity and broaden their usefulness in an increasing number of biomedical and industrial applications, while ensuring affordability. One major research interest is the miniaturization of sensors that has improved the performance of biosensors, microfluidics and signal processing. It also made it possible to have portable, low cost, and highly sensitive nano-biosensors [1].

1.1 Biosensors

The main characteristics of an effective biological sensor are sensitivity, specificity, stability multiplexing, fabrication simplicity and cost efficient [2]. All the characteristics are defined in Table 1.

Table 1: Definitions of the main characteristics of an effective biosensor

Characteristic	Definition
Sensitivity	The minimum amount of analyte detected by the sensor
Specificity	The ability to distinguish the desired sample in a mixture of different samples
Stability	The response of the sensor to the ambient disturbances and noise in and around the sensor
Multiplexing	The detection of multiple biomarkers, thus pathogens from a single sample
Measurement complexity	The number of involved off chip infrastructure and sample processing steps

Sensitivity reduces the volume and concentration of the processed biological sample which is the most important characteristic for a biosensor [2]. Specificity prevent the interference of

the ambient environment that could cause drifts and false positives in the output signal [3]. Multiplexing increases the efficiency of the sensor by running multiple assays to detect different biomarkers from the same biological sample, saving the cost and time of patients and point of care. The miniaturization of biosensors to the nano scale improve the specificity and sensitivity of sensors, leading to single molecule detection such as in nanopore. Although the sensitivity of nano-biosensors is not better than the bulk measurements but it allows for the detection of the lowest limit of molecules, increasing the multiplexing ability [2]. Additionally, the reduction of the samples processing steps and the complexity of the biosensors in measurement and detection methods makes the sensor more likely to be successful and industrialized [2]. The implemented approach in this thesis focuses on improving the nanopore setup currently used in the field rather than the performance of the sensor. This work partially automates the setup to reduce the complexity associated with the currently used methods. Additionally, integrating droplet microfluidics with a nanopore sensor increases the multiplexing capability of the system.

There are various methods of detection in biosensors, such as optical detection, electrical, mechanical and electrochemical [4]. In nanopores the most common types of detection are electrical and optical methods. Optical detection methods have some limitation where the reduction of samples causes the reduction in the intensity of the signal [4]. Some optical methods require the interaction with the detected molecules, preventing the investigation of molecules interactions. Additionally, the ambient light noise optical techniques experience could limit their sensitivity [4]. On the other hand, electrical sensing reduces the complexity of the measurement setup, sample preparations and typically lower in cost [2].

Another way of categorizing detection method is via labeling. Labeling molecules includes chemical labeling such as florescence, isotopic and nanoparticles labeling [5]. While some might argue that labeling is the only way to sensitivity in nano-biosensors, the transition to label free sensors reduces the complexity of the sensor, eliminating the labeling preparation step and the alteration of molecules intrinsic properties caused by labeling [5]. While labeling certainly has its advantages, label-free detection methods allowed for the study of biomolecular interactions using biosensors. Moreover, they eliminate false positives resulting from labeling methods and are more reproducible [5]. Therefore, moving to a more versatile label-free sensing technologies might be a way for direct and simpler biosensor technologies [6].

1.2 Nanopore sensors

Nanopore sensors are electronics-based devices capable of detecting single molecules. In the 1940's Wallace H. Coulter proposed the Coulter principle, which has evolved in recent years to revolutionize the field of biophysics [7]. It is the principle behind hematology, cell counting, and cell and particles characterization [8]. The coulter principle states that as particles move through an orifice surrounded by electrolytes, as presented in figure 1A, the particles create a partial blockage in the passing ionic current. A blockage can be visualized with a spike on a time vs current graph, as shown in figure 1B. The change of the ionic current signal across the orifice, made particle counting possible and eventually led to the development of coulter counters [7].

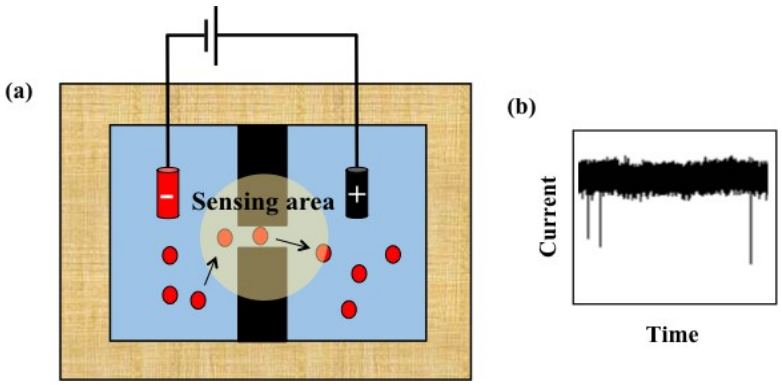

Figure 1: a) Coulter principle, when voltage is applied across a submerged orifice in electrolyte, charged particles traverse from one side to the other, causing a decrease in the readout current. (b) Ionic current measurement of the coulter counter, showing spikes when particles move through the orifice.

The amount of time and effort medical specialists put into counting red blood cells, was the motivation behind the Coulter's principle. The need for a reliable and reproducible cell counter became more evident post-World War II, due to increased necessity of repeated blood measurements as people recovered from radiation poisoning [9]. The Coulter counter started from creating an orifice in a cigarette wrapper cellophane using a hot needle. The cellophane was not very durable, but several cells were counted successfully [9]. By having the access to new technologies allowed us to make small holes with high precision, the Coulter counters have evolved and improved to pave the way for nanopores. Nanopores are predicted to be the future of DNA sequencing by monitoring the ionic current overtime for the passing DNA through a nanopore [6]. The sensitivity and specificity of nanopores make them one of a number of sequencing technologies that are poised to meet the challenge of the genome sequencing for less than $1000 [6].

Nanopore sensors rely on the action of driving DNA or protein molecules using electrophoretic forces through a pore in the nano scale [6]. The movement of a DNA or a protein molecule through the nanopore is called translocation [10]. The future vision of DNA sequencing using

nanopores is fiendishly hard due to the fast translocation of a single nucleotide though the pore, which is approximately one nucleotide per microsecond [6]. Therefore, the fast translocation of the four nucleotides are likely to be overwhelmed by thermodynamic fluctuations [6]. Additionally, a long DNA passing through a nanopore doesn't translocate the same way as eating a spaghetti, it folds into different hairpin conformations, making it difficult to probe individual nucleotides [11]. In order to achieve single nucleotide sensing, two goals have to be reached: the development of highly sensitive electronics with sufficient temporal resolution to distinguish individual bases, and the ability to perform long reads of polymers up to centimeters in length, such as the human genome [6].

Current applications of nanopores focus on DNA and gene detection by creating different shapes and geometries using binding sites and substrates to alter the original conformation such as in the art of DNA origami [12]. The label-free electrical sensing of nanopores abilities allowed the investigation of protein-protein interactions and protein folding [13]. Future applications might include concentrating diluted samples and combining biosensors within microfluidics, which will expand the range of nanopore applications.

1.3 The physics of Nanopore sensors

Nanopore sensors are single biomolecules sensors that rely on the Coulter principle, where a nano-scale aperture is sandwiched between two reservoirs of aqueous salt solution (typically KCl or LiCl). Each reservoir contains an electrode, such as AgCl, to apply an electrical potential difference across the nanopore and thereafter measure the ionic current through the pore. The translocation of a DNA molecule through a nanopore is shown in figure 2A The translocations of biomolecules across the pore create spikes in the baseline current, as presented in figure 2B. Each spike corresponds to a single DNA molecule translocating

through the 12 nm pore as in figure 2C. The magnitude of the ionic current reduction (ΔI) from the baseline for a single translocating molecule correlates to the molecular cross-sectional area of the molecule [10]. While the duration (dwell time) of the reduction is related to the length of the molecule [10].

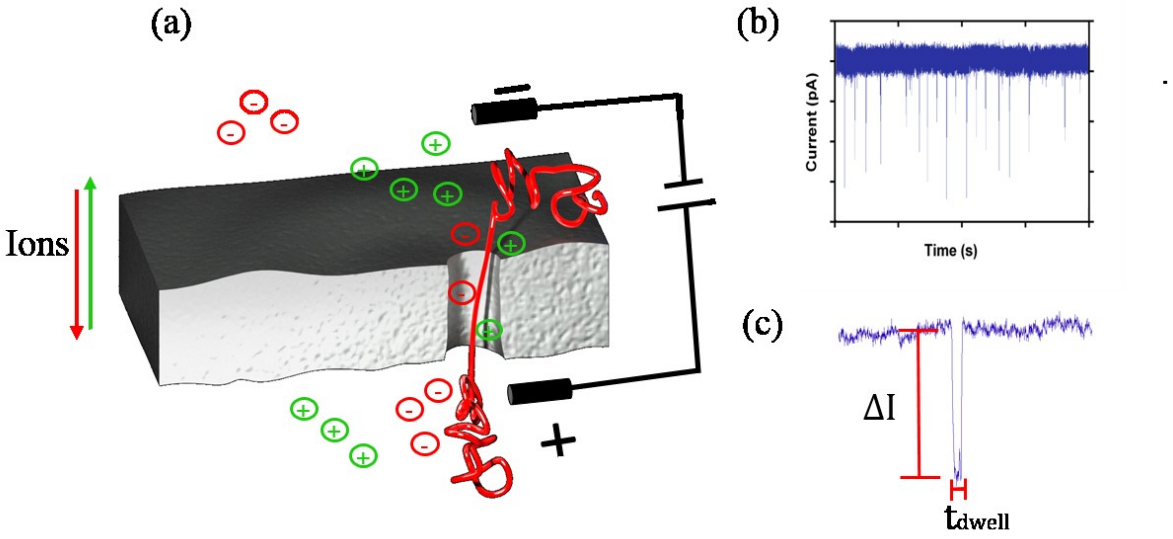

Figure 2: (a) DNA translocating through a nanopore causing the displacement of ions, (b) Electrical measurement of traces of multiple DNA molecules traversing through a 12 nm nanopore, (c) ΔI is the blockage depth and t_{dwell} is the time required for a single DNA to translocate through a nanopore. Measurement is from Axopatch 200B current amplifier with applied bias of 400 mv.

Nanopores are categorized into biological nanopores, synthetic nanopores, and a combination of the two. Biological nanopores are found in biological living organisms and they are either proteins or ion channels [14]. The fragile nature and short lifespan of biological nanopore led us to focus on integrating synthetic solid-state nanopores within microfluidic devices due to their convenient fabrication, and higher integrity.

The small size of nanopore sensors make them capable of detecting single molecules exclusively from purified and processed DNA or protein samples. The impurities in biological

fluids such as saliva and blood typically clog the pore, rendering it unfunctional. Therefore, the integration of a nanopore sensor within a microfluidic chip is essential to reduce the complexity of sample preparation and infrastructure setup prior to sensing. The automation of samples preparation, purification, and pre-processing afforded by microfluidics devices will be time and cost efficient, and more effective than current methods [15].

1.4 Microfluidics

Microfluidics science is the design and manufacturing of microchannel networks, to study, control and manipulate fluids in the microscale [16]. Microfluidics offers new and efficient therapeutic and diagnostic approaches in analytical chemistry, molecular biology, electronics and diagnostics [17]. The interest in microfluidics increased to deliver higher throughput, resolution, sensitivity, and sample and reagent reduction in cell counters [18]. The first motivation for the vast growth in microfluidics was in the 1980s due to the rise in interest in genomics and molecular biology [18]. The second motivation was in the 1999s, when the power and the potential of microfluidics became evident to the US military [18]. Therefore, they funded a series of research projects for the development of microfluidics deployable diagnostic devices, in order to test for chemical and biological threats in war zones [18]. The third motivation was the result of the great success in microelectronics industry, which translated to microfluidics in the use of lithography on silicon wafers and glass [19]. The first-generation microfluidics devices were made from glass and silicon, which prevented the use of any optical measurement techniques [20]. Therefore, the fabrication materials evolved to better suit biological applications such as the use of elastomers [19]. The elastic nature of elastomers notably surpass glass in fabrication in making on-chip pumps and valves to direct and manipulate fluids [18]. In the next generation of microfluidics devices, elastomers such as

poly-dimethylsiloxane (PDMS) became very popular because of their flexibility and lower cost of fabrication.

1.4.1 PDMS Physical and Mechanical Properties

The use of PDMS is seen in contact lenses, ear and nose implants, catheters, artificial skin, and various medical and environmental devices [21]. PDMS is chemically insert, biocompatible to a certain extent, permeable to gas and operationally functional within a wide range of temperatures (-45 to 200°C) [22]. Additionally, PDMS is optically transparent down to 280 nm wavelength, which makes it well-suited for various optical detection schemes such as UV light and fluorescence [21]. During fabrication PDMS solidify at low temperatures (70°C for 40 minutes) and can permanently bind to itself and a number of different materials, by forming covalent bonds when plasma treated [23]. In various applications, it is shown that PDMS can be chemically modified using chemical solutions, temperature, and plasma treatment [22]. Finally, PDMS is FDA approved as a food additive, which facilitate the approval process for PDMS based-biomedical applications.

1.5 Droplet Microfluidics

A subcategory of microfluidics is droplet microfluidics which is the creation of isolated fluidic droplets within microchannels. Droplet-based microfluidics emerged from two complementary motivations. The first one was creating microreactors for micro total analysis systems (μTAS) studies that provides the ability to mix and manipulate fine controlled droplets [38]. The second motivation came from the need for generating micro and nanodroplets for material science research for food and pharmaceutical applications [24]. The idea of compartmentalization of fluids as chemical and biological microreactors has already been

studied and discussed in literature long before the emergence of microfluidics [25]. Nonetheless, microfluidics facilitated the generation of confined droplets in microchannels and provided fine control over droplet size [38]. Droplet microfluidics helped with the isolation of biological and chemical reactions from the outside environment, specifically the surface of the microchannel [24].

Single flow (one phase) in microfluidics allow great control in flow properties; however, increasing the number of samples or reactions, enlarges the size of the device significantly [26]. Therefore, the use of droplet microfluidic enhances the multiplexity of microfluidics by enabling the parallel analysis of the same samples. This results in large data sets that efficiently save time and resources without the need for a design change or a larger device [27]. Additionally, the ratio of surface area to sample volume in droplets enhance the mixing properties in microfluidics, which decreases the mixing time [26].

The compartmentalization of fluids within droplets, increases the local concentration of molecules, which is capitalized in droplet digital polymerase chain reaction (ddPCR) for example. In ddPCR the sample is split into hundreds of nanoliter partitions (droplets) that allow the identification of single mutations in a fraction of a cell population that is important in many basic research and clinical diagnosis [28]. The mutation detection in regular PCR methods is when the mutation presence is 20% of the cell population, while ddPCR enhance the sensitivity to detect mutations in a 0.1% of the cell population [28].

1.5.1 PCR mechanism of work

Polymerize chain reaction (PCR) is the main amplification technique in laboratories, hospitals, and clinics, due to its reliability, stability, and consistency [29]. In the PCR sample mixture, there is an abundance of nucleotides, a complementary specific sequence for each DNA strand

called primers, the polymerase enzyme, and the sample [30]. PCR relies on high temperatures (95°C) to denature the double-stranded DNA [32]. Next, when the two strands are separated, the primers bind to their complementary regions (annealing process), which happens around 48-72 °C [31]. Annealing gives the polymerase enzyme a starting point to extend the two DNA strands using the free nucleotides in the solution [30]. Finally, the temperature cycling is repeated until the amplification is completed.

1.5.2 Amplification in Microfluidics Devices

Early 2000s Notomi *et al* invented loop mediated isothermal amplification (LAMP) that does not require temperature cycling as in PCR [32]. This feature makes LAMP an ideal candidate for microfluidics application. The temperature cycling step required by regular PCR adds complexity while LAMP employs a set of 4-6 primers instead of two and a Bst DNA polymerase enzyme to carry on the amplification at 65 °C [32]. The results of LAMP can be detected visually due to the white calcium precipitate of the chemical reaction [33]. Equation 1.1, 1.2, and 1.3 shows the amplification reactions where dNTPs are the free nucleotides in the reaction mixture [34].

$$(DNA)_{n-1} + dNTP \rightarrow (DNA)_n + P_2O_7^{4-} + 2H^+ \quad 1.1$$

$$P_2O_7^{4-} + 2Mg^{2+} \rightarrow Mg_2P_2O_7 \downarrow \quad 1.2$$

$$2Tris + 2H^+ \rightarrow 2Tris - H^+ \quad 1.3$$

Based on the by product $Mg_2P_2O_7$ in equation 1.2 the conductivity of the solution decreases due to the precipitation of ions, and the consumption of the free nucleotides [34]. The

conductance drop is due to the reduction in the charge carriers of the solution [34]. The conductance change can be used as an indicator for the amplification success in a nanopore-microfluidic setup by measuring the conductivity of the solution. In the appendix of this thesis, some preliminary data of integrating the application of LAMP into droplet microfluidics is presented.

1.6 Project Objectives

The integration of solid state nanopore sensors within microfluidics was achieved by Tahvildari *et al.*, 2015 [15]. The novelty of this project is to incorporate a nanopore sensor within a droplet microfluidics platform. Sample manipulation is just as important as having a sensitive sensor. Sample compartmentalization using droplets isolate small volume samples, reducing background interference and increasing the multiplexibility of the system.

The project is divided into three objectives, the first objective as presented in Chapter 2 is compartmentalizing liquids within droplets creating a stable and consistent segmented flow regime. Therefore, Chapter 2 presents the contributed forces to the segmented flow, and the design process of the droplet microfluidic device. The second objective of the project is to measure the conductance of aqueous droplets. Therefore, in Chapter 3, we present the electrodes' choice for the droplet microfluidics device and a research problem related to the electrical contact between droplets and electrodes in the presence of oil in segmented flow. The conductance measurement of droplets is crucial for nanopore integration. In order to be able to apply a voltage across the droplet and across the membrane, the electrodes need to have a direct contact with the conductive droplets. Then, Chapter 4 discusses the integration between droplets-based microfluidics with a nanopore sensor, and DNA molecules sensing

within droplets using a nanopore. Finally, Chapter 5 presents the conclusions and an outlook of applications that can utilize the developed platform.

Chapter 2 Droplet-based Microfluidics

Droplet-based microfluidics is the creation of droplets or emulsions by any geometry that leads to droplet formation. The most used geometries are T-junction and flow focusing designs [35]. The schematics of a T-junction and a flow focusing devices are shown in Figure 3A and B, respectively. Droplets or emulsions are the result of the interaction between two immiscible fluids subjected to a pressure gradient, typically called the dispersed phase which becomes droplets and the continuous phases that carries droplets [36].

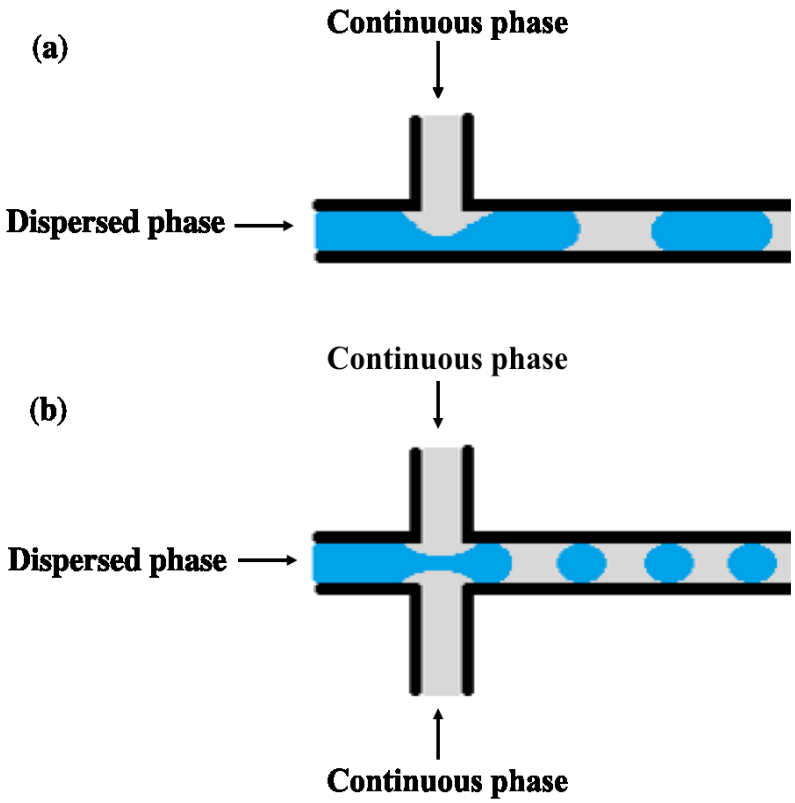

Figure 3: Geometries of (a) T-Junction design, (b) Flow focusing design

Droplet microfluidics has many advantages that makes them extensively employed in various fields including drug delivery, stem cells research, molecular biology, nucleic acid amplifications, environmental testing, protein crystallization, cell encapsulation and imaging [37]. The traditional methods use samples in the millilitre range, while the use of droplets in microfluidics reduces the volume of samples to the nano- and picolitre range [37]. The reduction of sample volume and reagents speed the chemical and biological reaction times, subsequently reducing cost [38]. The main advantage of using droplets in microfluidics is the fine control of samples, which increases the detection sensitivity and the local concentration of samples such as in droplet digital PCR (ddPCR) [38]. Moreover, droplets enhance the mixing of samples and reagents inside micro-channels by reducing the time of heat and mass transfer due to the smaller confined volumes [38]. The precise control and manipulation of droplets prevents cross-talking, which allows the processing of different samples simultaneously [39]. Simultaneous chemical reactions and detection within droplets is done by the generation of series of droplets containing the same mixture and then detected by imaging and optical methods [40]. Chen et al. demonstrated the detection of DNA in more than sixteen droplets simultaneously using florescence labeling as a proof of concept [40]. Their systems demonstrate a higher throughput of biosensing than regular detection methods. Microdroplet systems are used for single molecule detection in molecular biology due to their low sample consumption and background noise reduction abilities. Biological biomarkers are collected in very low concentrations, which makes isolating and analyzing single molecules from complex biological mixtures extremely difficult if not impossible [41]. A study by Choi *et al.* reported a high throughput droplet-based system that is able to detect bovine angiogenin protein in cow's milk that requires 1 nl of sample by using florescence polarization [42]. In comparison to conventional microfluidics experiments, Choi *et al.* device showed a reduction

of 10 folds in dead volumes, which shows the capabilities of droplet-microfluidics when combined with different detection methods.

Another study successfully developed a sensor that detects glucose concentrations using a flow focusing design to generate water-air droplets, where glucose oxidase enzyme is incorporated in the device for the glucose sensing [43]. The study also showed that fluorescence densities linearly increased with glucose concentrations up to 3 mM and the incorporation of the glucose oxidase enzyme in the microchip reduced the detection limit to 6.64 μM which is an improvement over the most sensitive reported paper-based electro- chemical flow-injection method with 0.2 mM detection limit [44]. The incorporation of different chemical reactions and biosensors within droplet-microfluidics is constantly showing an improvement of detection sensitivity, proving the capabilities of this approach. Furthermore, therapeutic approaches using encapsulation had demonstrated the strength of droplet microfluidics technology. Geng *et al.* demonstrated in their recent work on water-oil-water emulsions the ability of encapsulating individual cells to serve as microreactors for PCR assays [42]. On site diagnostic droplet microfluidic chips are in demand due to their convenience and lower cost for forensics and point of care [37]. An example of diagnostic chips is the device developed by Wali *et al.* for cocaine detection using saliva samples. The chip showed two to three folds increase in extraction efficiency from the standard commonly used H-filters [45]. Similarly, Parakash *et al*. illustrated a real time-PCR chip for detecting influenza A and C viruses. The device requires ~ 5 copies of a gene for detection and 95% PCR efficiency, which is comparable to top bench equipment [46]. This is possible due to the aforementioned characteristics of droplet microfluidics, the fast kinetics reactions due to the small sample and reagents volumes and the reduction of the background noise [46]. The previous study shows

the promising capabilities of microdroplet devices for pathogen detection and an alternative to traditional and time-consuming top bench methods. Numerous studies have shown the potency of droplet microfluidics, however, there is a lot of challenges left to be addressed in order to capitalise a truly robust real-life droplet microfluidic device [37]. Many popular lab-on-a-chip devices in microbiology rely on florescence as a mean of detection, however, the use of florescence has its drawbacks [47]. While an active field of research is developing more dyes for different microorganisms, the immigration to label-free detection methods can reduce the complexity of the fabricated devices [47]. Additionally, many of lab on a chip devices are one-time use, therefore more work needs to be done to increase the durability and multiplexing capabilities of these systems. Another challenge is the reagents concentrations throughout reactions, some studies incorporated the use of valves and optical feedback loops to monitor and change reagents concentrations, however controlling the concentration throughout reactions remains a challenge [47]. Finally, the complexity of the fabrication and usage of droplet microfluidics devices should be carefully considered in order to be industrialized [47].

Droplet microfluidics have the capabilities of significantly reducing the volume of the required samples, cost and time of biological tests in molecular biology, forensics and medicine. Future applications and devices could revolutionize the field of therapeutic and diagnostic microfluidics [37].

2.1 Forces in Segmented Flow

Segmented flow (creation of microdroplets) results from the interaction between two immiscible fluids. Forces involved in the formation of a droplet regime is crucial in predicting and designing a multiphasic micro-channel system [36]. The different types of flow are the result of the interfacial, viscous, inertial and gravitational forces, in addition to the surface

wettability characteristics [36]. However, with channels at the micron level, the interfacial forces largely dominate over inertial and gravitation forces, rendering them negligible [36]. The relationship between interfacial forces and gravity is explained by the Bond number (Bo),

$$Bo = (\Delta\rho) g d_h^2 \sigma^{-1} \quad 2.1$$

In equation 2.1 $\Delta\rho$ represents the difference in density between the two selected immiscible fluids (oil and aqueous solution), while d_h in the hydraulic diameter of the microfluidic channel ($d_h = {}^{4A}/_{\Gamma}$), where A is the cross-sectional area and Γ is the wetted perimeter. In microfluidics Bo number is generally $Bo \ll 1$ [48]. Therefore, in microfluidics the channel dimensions have to be carefully considered to have dominant interfacial forces in the system.

Another important dimensionless number to consider is the capillary number (*Ca)* that represents the ratio of viscous forces to surface tension in a segmented flow.

$$Ca = \frac{\mu U_d}{\sigma} \frac{\mu}{\mu_d} \quad 2.2$$

In equation 2.2, σ represents the interfacial tension, μ and μ_d are the viscosities of the continuous phase and the dispersed phase, respectively and U_d is the velocity of the dispersed phase. The Capillary number is used in this thesis to predict the desired flow regime.

Another consideration is the Weber number (*We*), which illustrates the ratio of inertia to surface forces. In microfluidics applications *We* number is typically $\mathrm{We} < 1$ [48]. The Weber number is useful and carefully considered in larger channels and high flow rate applications where inertia forces are significant [35].

$$We = \frac{\rho U_d^2 d_h}{\sigma} \quad 2.3$$

For continuous single flow (one phase), the Reynolds number is the ratio of the capillary and Weber numbers, which relates vicious and inertial forces. Its value is fixed for a specific weber and capillary number.

$$\mathrm{Re} = {We}/{Ca} \quad 2.4$$

A Reynolds number (Re) less than 1 ensures a laminar flow of fluids inside microfluidic channels as in figure 4 [35].

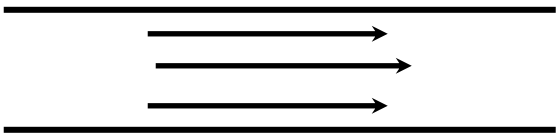

Figure 4: Laminar flow

According to equation 2.2 and 2.3, the interfacial forces dominate in microscale channels unless U_d is in the orders of meters per seconds which creates a very unstable regime and interfacial forces.

A recent study by Gataski *et al.* shows that droplets breakup in T-junction designs is not caused by shear stress rather by the increased capillary number caused by the pressure drop between the emerging droplet [35]. Understanding the forces causing the different flow regimes allow an accurate prediction of the flow type and helps in maintaining a stable flow [49].

The two most important variables to consider when designing a T-junction microfluidics device are the channel size and the velocity of the dispersed phase as seen in figure 5. These variables are important to ensure the dominance of the interfacial forces over inertial, viscous and gravitational forces. The designed device dimensions used in this thesis are extracted from figure 5 elaborate diagram [50]. The device used in this thesis has a channel width of 200 μm and the average segmented flow velocity is maintained at 1.8 mm/s, which ensures a capillary number of 10^{-3}, bond number of 0.42×10^{-3} and weber number of 0.7×10^{-5} . Operating in this range ensure the dominance of interfacial forces over inertial and gravitational forces. Additionally, the Reynold's number for the fabricated device is 0.01 which maintains a laminar flow in the system.

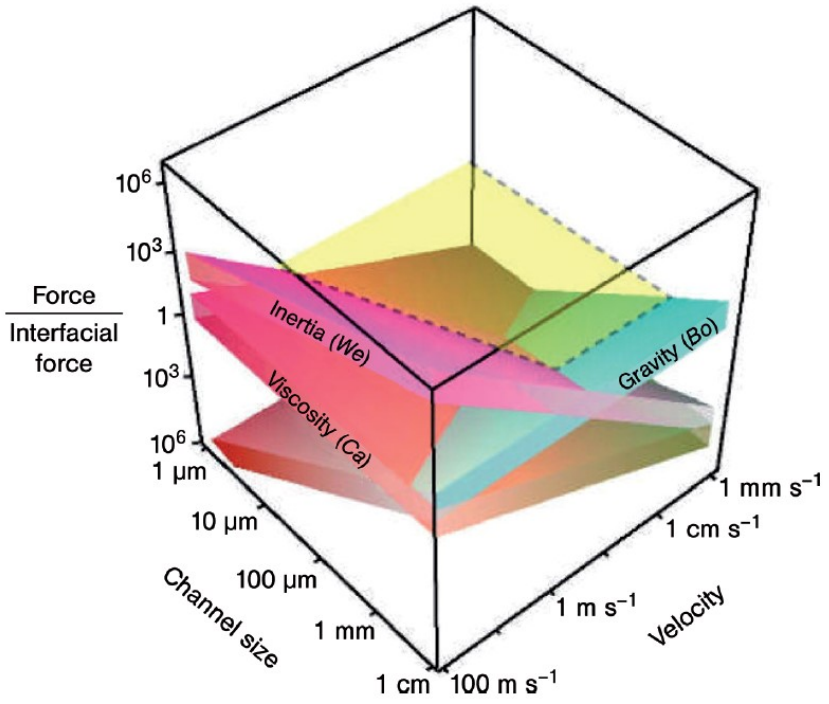

Figure 5: The effect of the capillary (*Ca*), Weber (*We*), and bond numbers expressing the relation of the inertia, viscous, and gravitational forces with respect to interfacial forces in droplet microfluidics systems expressed by channel size and the velocity of the dispersed phase. The yellow plane shows the condition when all the forces indicated numbers are equal to 1(reproduced from [50]). The calculated capillary number for the device used in this thesis is 10^{-3}, bond number of 0.42×10^{-3} and weber number of 0.7×10^{-5}.

2.2 Droplet Formation and Different Flow Regimes

Various flow regimes can be obtained by manipulating the *Ca* number by changing the flow rate ratio of the continuous and dispersed phase (Q_c/Q_d) [35]. The main types of biphasic flow in T-junction devices are jetting, squeezing and dripping [35]. In addition to the *Ca* number, channel surface properties play a crucial role in droplet formation. To form droplets and break up the two immiscible fluids in gas-liquid microreactors the channel surfaces are usually hydrophilic while they have to be hydrophobic in oil-liquid droplets [50].

2.2.1 Jetting, Squeezing and Dripping at T-junction Geometry

The first observed flow regime in a T-junction geometry device is squeezing, where the generated droplets conform to the size of the channel until pressure drops across the droplet causing the pinch off by the continuous phase as shown in figure 6A [49]. The second regime is dripping as in figure 6B, where droplets are smaller than the dimensions of the main channel and are pinched off due to shear forces and higher *Ca* [35]. The third regime is jetting, which is classified into two forms of flow:

1- The flow of one fluid creating an unstable thread or a jet that narrows away from the tip of the junction until it pinches off like in figure 6C [49].
2- The co-flow regime of two fluids flow side by side shown in figure 6D, which occurs at higher flow rate [46].

Based on equation 2.2, at higher flow rates of the dispersed phase, the viscous forces dominate resulting in the co-flow jetting regime [51].

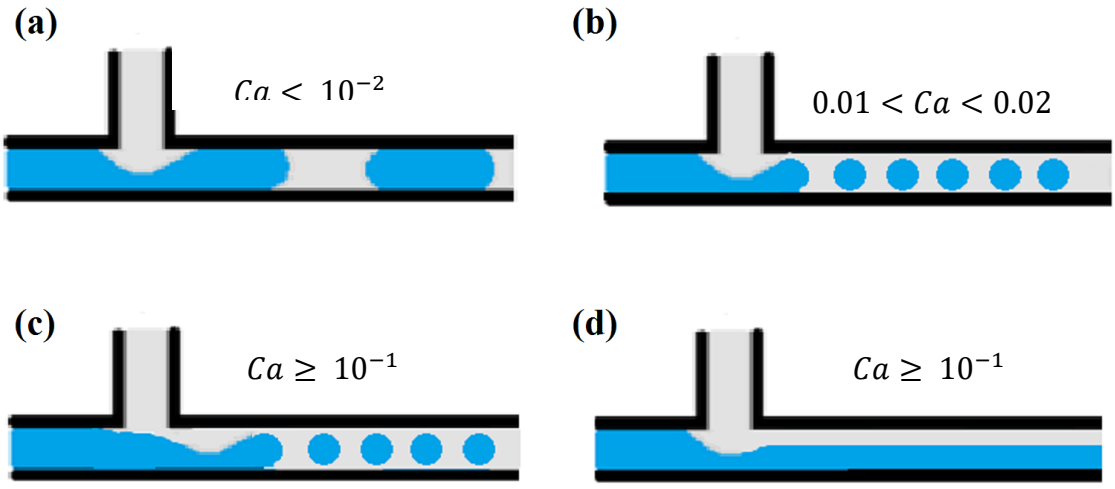

Figure 6: (a) squeezing, (b) dripping, (c) jetting, (d) jetting: co-flow [52][49][53][54].

To summarize, the squeezing and dripping flow regimes act on lower capillary numbers where interfacial forces are dominant, while the jetting flow happens at a higher flow rates where the viscous forces dominate [52]. The different flow regimes in a T-junction occur when $Ca < 10^{-2}$ for squeezing, $0.01 < Ca < 0.02$ for dripping, and $Ca \geq 10^{-1}$ for jetting [55] [52]. The Capillary number is important to predict the desired flow regime. In this thesis the surface tension between mineral oil and water is 0.05 N/m [56], $\mu_d = 0.017\ Pa.s$ (Mineral oil, Sigma-Aldrich), $\mu_c = 0.001\ Pa.s$, $U_d = 0.0018\ m/s$, therefore as mentioned earlier the calculated capillary number is 10^{-3} which ensures the desired squeezing regime in the fabricated devices.

2.3 Surface Modification

Methods for increasing or decreasing the wettability of fluid channel surfaces has been extensively discussed in literature. Such methods are plasma treatment, saline treatment,

radiation exposure as to UV light, surface polymer deposition and chemical reactions [50]. The surface wettability has to be compatible with the continuous phase to prevent the cross contamination between droplets. Additionally, surface modification eliminate flow instability by controlling for interfacial forces allowing for a stable flow of gas-fluid or fluid-fluid droplets [57]. Surface modifications on PDMS are often temporary, resulting in shorter lifespan of applications relying on surface modification, which has limited the expansion and the use of PDMS devices [57].

2.4 Experimental Setup

2.4.1 Fabrication – Soft Lithography

PDMS-based molds are fabricated using photolithography methods [58]. Lithography is a 3D patterning method done by transferring specific features into a substrate through etching [59]. Etching is the process of chemically removing layers of photoresist from a wafer, and it can be done by using photolithography [59]. Photolithography is the use of light on photoresists to transfer features. Light exposure either soften (positive) or harden (negative) the resist, yielding it more or less soluble in the developer, respectively [58]. Photoresists can give different thicknesses, edge shapes and optical properties [60]. Development of the mold starts with designing a binary (black and white) mask. The features on the mask are then transferred to photoresist through hard contact lithography [59]. Next, they are exposed to UV light for a given time (calculated based on the thickness of the photoresist and the power of the UV source) to initiate the polymerization chemical reaction in the photoresist as seen in figure 7 [58]. The 2D photomasks are usually designed using CAD software; in this project AutoCAD (Autodesk, version O.48M.299) was used. After that, soft-lithography is done as seen in figure 7 by casting incurred PDMS on the mold, then exposed to 75°C for at least an hour.

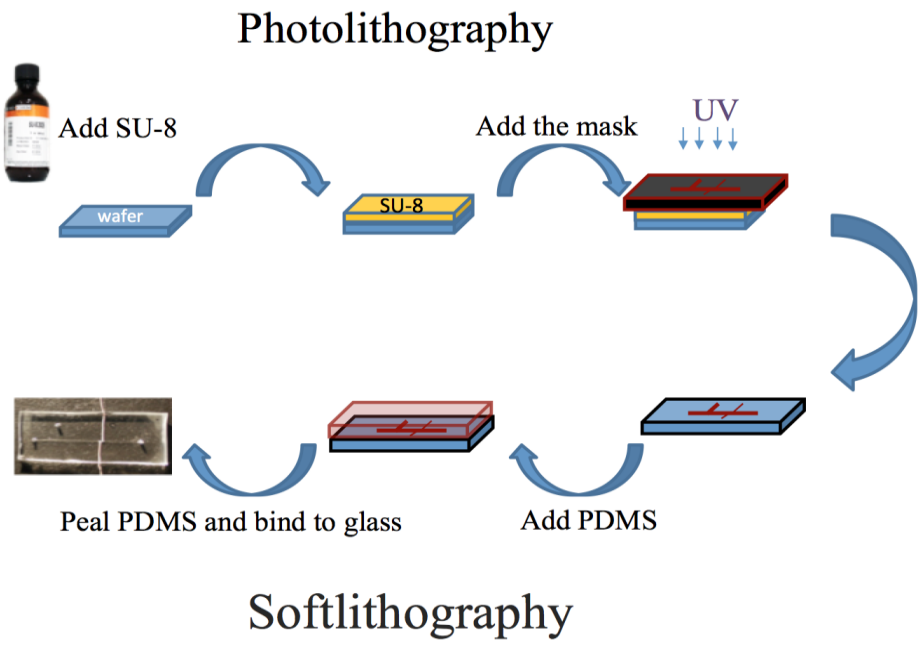

Figure 7: The process of photolithography and softlithography.

2.4.1.1 Negative photoresist: SU8

SU8 is a chemically stable negative tone photoresist, which cross-links when exposed to UV light. All negative photoresists are composed of a rubber material and a photoactive agent dissolved in an organic solvent [61]. Similarly, SU8 is made of the chemical compound EPON® SU-8 resin (MicroChem) dissolved in an organic solvent. The percentage of the organic solvent determines the viscosity, thus the final thickness of the photoresist achievable with spin-coating. This thickness could range from sub-micrometer to millimetre [62].

2.4.1.2 Positive photoresists: AZ50X

AZ50X (Electronic Materials®) is a positive tone photoresist in which UV radiation makes the exposed areas more soluble in the developer. All positive resists are composed of a resin, an active photo compound and a solvent [61]. Unlike negative tone resists, positive photoresist are often thermosets, allowing the features to melt to create rounded geometries when exposed

to heat. This is specifically useful in making compatible features with the use of valves in microfluidics devices [61].

2.4.2 Wafer Fabrication

The first step of mold fabrication is cleaning the silicon wafer from any dust or biological contaminants by rinsing with isopropanol (IPA), acetone, and ethanol, then blow-drying the wafer with pure N_2 gas. Subsequently, the wafer is plasma treated using an oxygen plasma (AutoGlow Research) for 5 minutes at 200W and placed on a hot plate at 200° Celsius for 10 minutes. The plasma treatment is done to guarantee the evaporation of liquids and to make the photoresist film non-sticking to the mask during exposure. Next, approximately 1 mL of negative photoresist is added to the wafer and spin-coated to achieve the desired thickness; all the thicknesses used in this thesis are outlined in tables 2, 3 and 4. Consequently, the wafer is soft-baked at 65° Celsius and 95° Celsius on a hot plate for a duration calibrated by the manufacture for each thickness and then cooled down for 5 minutes. Soft bake is performed to prevent resist contamination and the mask from sticking to the resist. Additionally, it avoids foaming and bubbling from N_2 during UV exposure and during post bake step. It also hardens the resist by evaporating some of the solvents to maintain the spin coated thickness. Furthermore, in case multiple layers are required, it prevents the melting of the first resist layer. Next, the designed mask is placed on the wafer with the hard contact option using OAI DUV/NUV mask aligner (Model 206), then the specific features on the mask is exposed to UV light. The wafer is then post baked at 65° Celsius and 95° Celsius for a calibrated duration for the desired thickness. In this project all the soft-bake and post-bake durations are used following the manufacturer instructions (MicroChem). Following the post-bake, the wafer is cooled down for 3-5 minutes, and developed for 3-5 minutes until the features are clear. Then

the wafer is cleaned by rinsing with IPA and dried with N2 gas. Finally, the wafer is hard baked for 15 minutes at 150° Celsius on a hot plate to enhance crosslinking and solvent evaporation.

Positive photoresists require a rehydration step to restore the lost moisture from the photoresist during the soft-bake step. Unlike negative resists, the post-bake step for positive resists is done after developing due to the thermal sensitivity of AZ photoresists.

The final step of wafer preparation is adding 1.5 μL of Chlorosilane and placed in a vacuum for 5 minutes and for at least two hours without releasing the vacuum to initiate the silane treatment.

Table 2: Az50X (master mould fabrication parameters (65 μm height)

Spin	Soft bake	Rehydration	UV exposure	Developing	Reflow
5s at 500 rpm	2 min at 85° C	At least 3 hours	84 s	20 minutes	5 minutes at 75°C 5 minutes at 105°C 5 minutes at 135°C
30s at 1000 rpm	12 min at 115° C				
5s at 500 rpm					

Table 3: Su8 - 2050 (Microchem Inc.) master mould fabrication parameters (80 μm height)

Spin	Soft bake	UV exposure	Post bake	Developing
10s at 500 rpm	2 min at 65° C	12 s	2 min at 65° C	5 minutes
30s at 1050 rpm	9 min at 95° C		9 min at 95° C	
10s at 500 rpm				

Table 4: Su8-2050 (Microchem Inc.) master mould fabrication parameters (60 μm height)				
Spin	Soft bake	UV exposure	Post bake	Developing
10s at 500 rpm	2 min at 65° C	12 s	2 min at 65° C	5 minutes
30s at 1900 rpm,	9 min at 95° C		9 min at 95° C	
10s at 500 rpm				

2.4.3 Device Assembly

The material of choice for replicating designs on the master mould for experiments is PDMS. PDMS is a colourless relatively biocompatible polymer. Commercially sold PDMS comes in a kit (Sylgard 184 elastomer kit) with a base and a curing agent. The curing agent serves to facilitate cross-linkage of the liquid polymer for a quick solidification. The ratio used is 1:10 of curing agent to polymer, which results in medium PDMS hardness. The polymer and the curing agent are mixed thoroughly and then placed in a vacuum to remove trapped bubbles caused by the mixing. The degassed PDMS is then either casted or spin-coated based on the desired thickness on the fabricated wafer and placed in a vacuum to degas any extra bubbles. Next, the wafer is moved to a 70° C oven for at least an hour to solidify. All the spin-coated parameters used in this thesis are shown in table 5.

Table 5: PDMS Spin-coating parameters			
250 μm	200 μm	80 μm	40 μm
10s at 300 rpm	10s at 300 rpm	10s at 500 rpm	10s at 500 rpm
30s at 400 rpm	30s at 450 rpm	30s at 1050 rpm	30s at 2000 rpm
5s at 0 rpm	5s at 0 rpm	5s at 0 rpm	5s at 0 rpm

Subsequently, the PDMS coated wafer is then cut using a scalpel and slowly peeled off from the wafer. Then, holes are punched as shown on figure 8A on the marked circles in figure 8B to create inlets and outlet for fluids. Next, PDMS is sealed by binding it to a 25x75x1 mm glass slide using 50W for 36s plasma treatment.

2.4.4 T-Junction Device

T-Junction geometry is the chosen design for droplet formation due to the previously mentioned advantages. In order to create larger droplets that conform to the size of the channel with lower flow rates, many studies favoured T-junction geometry when lower flow rate applications are desired [59]. Flow focusing design as shown in figure 3B is preferred when higher flow rate and throughput of emulsions are desired. The width, height and length of the T-junction device main channel are 200 μm, 16 mm, 80 μm, respectively. The width narrows at T-junction to 100 μm to facilitate the pinch off of the dispersed phase as shown in figure 8B.

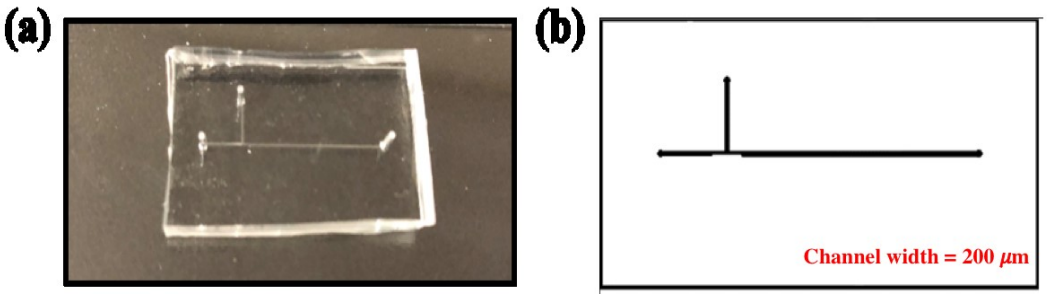

Figure 8: (a) T- junction PDMS device (b) T-junction design

After fabrication the device is left in the oven for 48 hours to increase the surface hydrophobicity to match the continuous phase hydrophobicity (oil). The two immiscible fluids used as continuous phase and dispersed phase are Mineral oil (0.84g/mL) and a 2 M KCl

solution, respectively. Fluids are prepared in 50 ml glass vials with a needle inserted through the septum to connect manual pressure regulators (Marsh Bellofram Type 10) to drive fluids into the channel. Fluids are delivered to the device via PTFE soft tubes.

Aqueous droplets in oil were chosen over gas-liquid to prevent cross contamination between aqueous samples. liquid-liquid droplets especially oil-KCl isolate the droplets from the outer environment. Additionally, it is a much sustainable regime in terms of droplets size and flow rate.

2.5 Results and Discussion

The biphasic segmented flow was achieved successfully. The dimensions of the device are critical parameters in the designing stage to form stable droplets. The *Ca* number should be less than 10^{-2} and *Re* number less than 1 to guarantee a laminar flow where interfacial forces dominate [49]. The pressure driven immiscible fluids were subjected to different pressures to achieve the desired regime. The pressure of the continuous phase was set on 1.5 Psi while the pressure of the dispersed phase is manipulated to stabilize the segmented flow regime which ranged between 1.8 Psi to 3.5 Psi depending on the desired flow rate and the size of droplets. The pressure of the dispersed phase was kept on the lower range to establish a lower flow rate and bigger droplets. The average droplets volume is 14.0 ± 0.4 nL with a speed of 1.8 mm/s which insures the squeezing regimes of the system.

The surface treatment done by incubating the device for 48 hours in 70º C oven is an essential step to increase the hydrophobicity of the wall channels. The hydrophobicity of the channels attracts oil forming a thin layer between the channel walls and the droplet, isolating it completely from the channel walls as seen in figure 9. The hydrophobicity is inspected visually by the ability to form stable droplets regime without the presence of KCl residue on

the sides of the main channel. The surface treatment ensures the creation and stabilization of the squeezing regime.

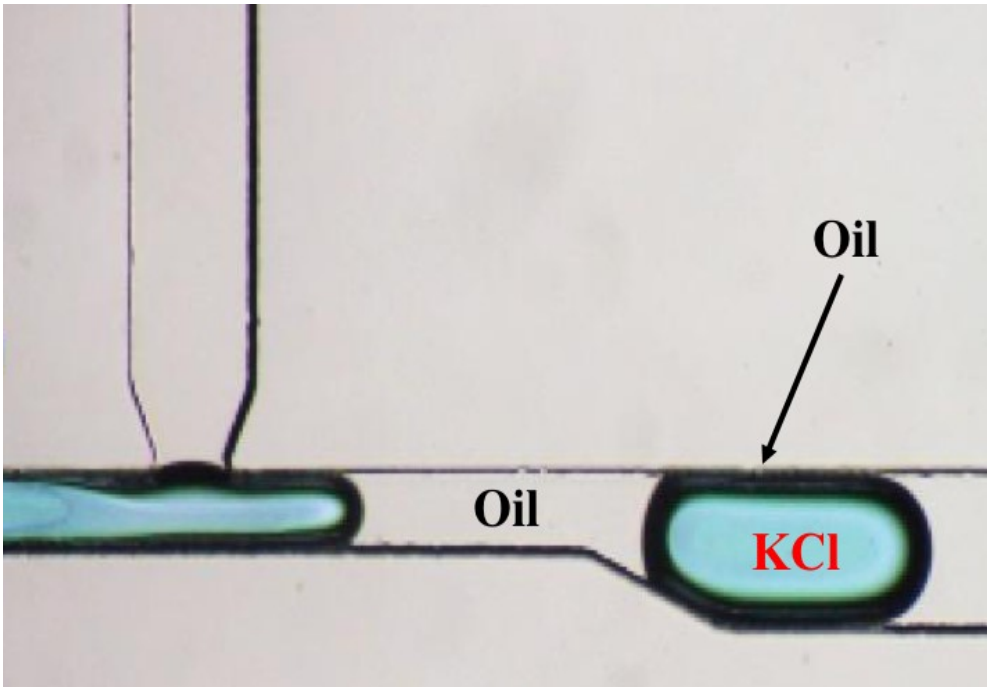

Figure 9: Oil-KCl droplets, where a thin layer of oil surrounds the KCl droplet

After the first objective of creating a stable and monodisperse segmented flow. Chapter 3 presents the second objective of electrodes integration into the T-junction device to measure the conductance of the passing droplets.

Chapter 3 Electrical Contact

Establishing the electrical contract between the segmented flow discussed in Chapter 2 and the electrodes embedded in the device is an important step in this project. This is particularly challenging due to the use of oil as a continuous phase, the main challenge to overcome in oil-KCl droplet sensing is the loss of conductance due to the thin oil film formed on the tip of the electrodes, preventing the sensing of the sequentially passing droplets. In this Chapter we explore varies strategies to ensure continuous impedance sensing of the segmented flow in the use of oil as a continuous phase.

3.1 Methodology and Experimental Setup

3.1.1 Electrodes Selection

The main characteristics of electrodes used in biological applications are reversibility, stability and reproducibility [49]. All three features are connected to the functionality of the electrodes, which means that the equilibrium of the chemical reaction should be maintained and not disturbed by any external or biological changes [49]. Electrodes are generally categorized into two main groups polarizable and non-polarizable [63]. Although both categories can be described theoretically, neither can be perfectly fabricated in practice. Polarizable electrodes operate by changing the distribution of the ionic charge around the tip of electrodes and do not allow an actual current to pass freely between the electrode-electrolyte interface [49]. While non-polarizable electrodes allow the free passage of current between the electrodes and the electrolyte via a redox reaction [63]. Redox reaction occurs between electrodes and the electrolyte until it reaches equilibrium without changing the distribution of ions on the electrode-electrolytes interface [64]. In other words, non-polarizable electrodes transfer the

electronic current to an ionic current by removing an electron from the metal and add it to an ion in the solution. While polarizable electrodes create a layer of access ions on the surface of the electrodes, which acts as a capacitor [27]. Although having perfectly non-polarizable electrodes in practice is not possible, it is feasible to have electrodes that closely behave with the same characteristics, such as AgCl electrodes [64].

In biological applications the charge distribution found adjacent to polarizable electrodes creates serious limitations when electrical measurements include low frequency or DC signals [27]. The movement in the ionic solutions will change the distribution on the electrode interface changing the electrode voltage, which results in motion artefacts [27]. Therefore, the most preferred electrodes in biomedical applications are non-polarizable electrodes such as AgCl electrodes, which are the electrodes of choice for the T-junction microfluidics device [27].

3.1.2 AgCl Electrodes Fabrication

AgCl electrodes are chosen for being stable, non-toxic, non-polarizable, good conductors, have low impedance and do not contaminate the surrounding media [27]. Additionally, they are relatively low in cost and extensively used in biophysics and biological measurements [27]. Since AgCl electrodes rely on a redox reaction for measurement as shown in equation 3.1 and 3.2, they have to be immersed in an electrolyte containing a soluble chloride solution of a known concentration such as 2M KCl or 0.1N HCl [64].

$$Ag_{(solid)} \rightleftharpoons Ag^{+}_{(solution)} + e^{-}_{(metal\ phase)} \quad 3.1$$

$$Ag^{+}_{(solution)} + Cl^{-}_{(solution)} \rightleftharpoons AgCl_{(solid)} \quad 3.2$$

AgCl electrodes are made by the incubation of stripped 200 μm Ag wire (Alfa Aesar™, 99.99% metal basis) in sodium hypochlorite (NaOCl; chlorine bleach) for 1-2 hours, which initiates the passive chemical reaction of converting the soluble state of chloride to a solid state by chemically interacting with silver wires [64].

3.1.3 Circuit Design for Impedance Sensing

The electrical circuit shown in figure 10 is composed of a function generator, low-noise preamplifier, transimpedance amplifier, lock-in amplifier and a customized code in LabVIEW developed for this experiment. An alternate current (AC) generated by the function generator is chosen to ensure the symmetry of the electrodes and to produce 10KHz frequency. The voltage generated from the function generator is sent to a unity gain low-noise preamplifier (Stanford Research Systems SR560) for signal stabilization. The input voltage is received by the first electrode and the output is read by the second electrode as seen in figure 10. The output current is converted to a voltage and amplified by a factor of 10^4 , 10^5, 10^7 depending on the signal via the transimpedance amplifier (Keithley 428). The signal to and from the device is carried through a BNC cable.

The amplified voltage is then sent to the lock in amplifier (Stanford Research Systems SR830 DSP) for detection. The lock-in amplifier extracts the specific waveform signal synced from the input frequency from the function generation, eliminating all other external noises. Finally, the lock-in amplifier signal is sent to a custom LabVIEW code through a 16- bit data acquisition (DAQ) card (NI PCI-6221; National Instruments) for viewing, real time observation and data recording.

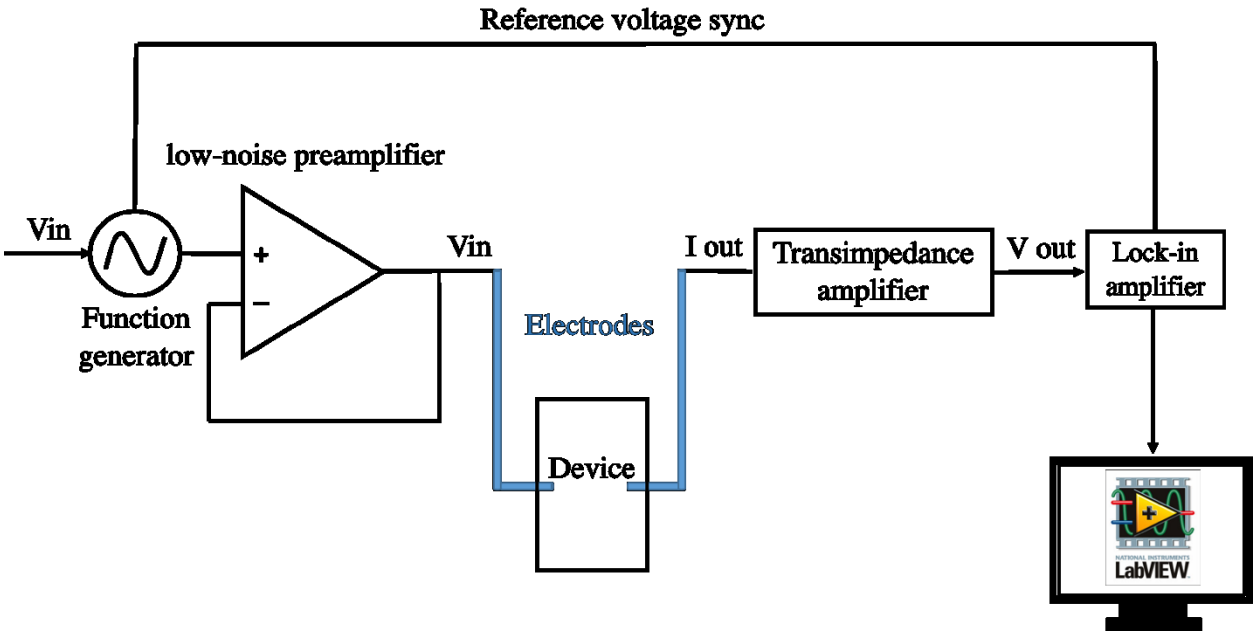

Figure 10: The electronics setup for the impedance measurement where voltage is generated through a function generator and then passed through a unity gain low-noise preamplifier to the first electrode of the device. The output current signal is then read out by the second electrode and converted to voltage and amplified by the transimpedance amplifier. The device signal is isolated using the lock-in amplifier and read by a 16-bit DAQ card, then viewed with a custom LabView code.

3.1.4 Electrode Design and Fabrication

Various electrode designs have been investigated for successful impedance sensing. In order to establish an oil free droplet-electrode stable electrical contact across the nanopore in the Droplet microfluidic-nanopore (DMN) device later on, an initial solid contact should be maintained between droplet-electrode interface.

The electrodes design as shown in figure 11A are inserted from the top of the main channel for droplets sensing, figure 11B shows a side view schematic of the electrodes. The electrodes are made by cutting 4 cm of a 250 μm diameter Ag wire, then the Ag wires are covered by ID: 840 μm, OD: 1.5mm, ℓ: 2 mm FEP sleeve (Upchurch Scientific). The empty space between the Ag wire and the FEP sleeve is sealed by injecting liquid PDMS. One side of the silver wire

is connected to a regular sleeved extension copper wire via soldering to increase the length and the stability of the electrode. The Ag – Cu connection is then covered with a PTFE heat shrink sleeve to give the electrode better firmness and stability. Next, the fabricated electrodes are left in an oven at 70° C for the PDMS to solidify. Then, the tips are cut to ensure a clean, and PDMS-free Ag surface between the electrode-electrolyte interface. Finally, the electrodes are immersed in bleach as described earlier to form the AgCl layer on the tips of the electrodes.

The second electrodes design as seen in figure 11C is fabricated by adding two side 200 μm channels for the electrodes to be manually inserted. The distance between the two electrodes channels is 500 μm to ease the insertion and allow the nanopore integration in the DMN design later on. The main channel narrows closer to the electrodes' insertion area by 50%, decreasing from 200 μm to 100 μm to elongate the droplets in the sensing area. This allow the electrodes-droplets contact with smaller droplets. Next, bare 250 μm Ag wires are inserted through the side channels as seen in the device's top view in figure 11D. The electrodes size is chosen because 250 μm electrodes have enough mechanical strength to handle the assembly process. Smaller sizes of electrodes such as 100 μm were very fragile to manually handle, they typically break during the device assembly. Additionally, this size is chosen to completely seal the side channels, preventing the leakage of the main channel fluids.

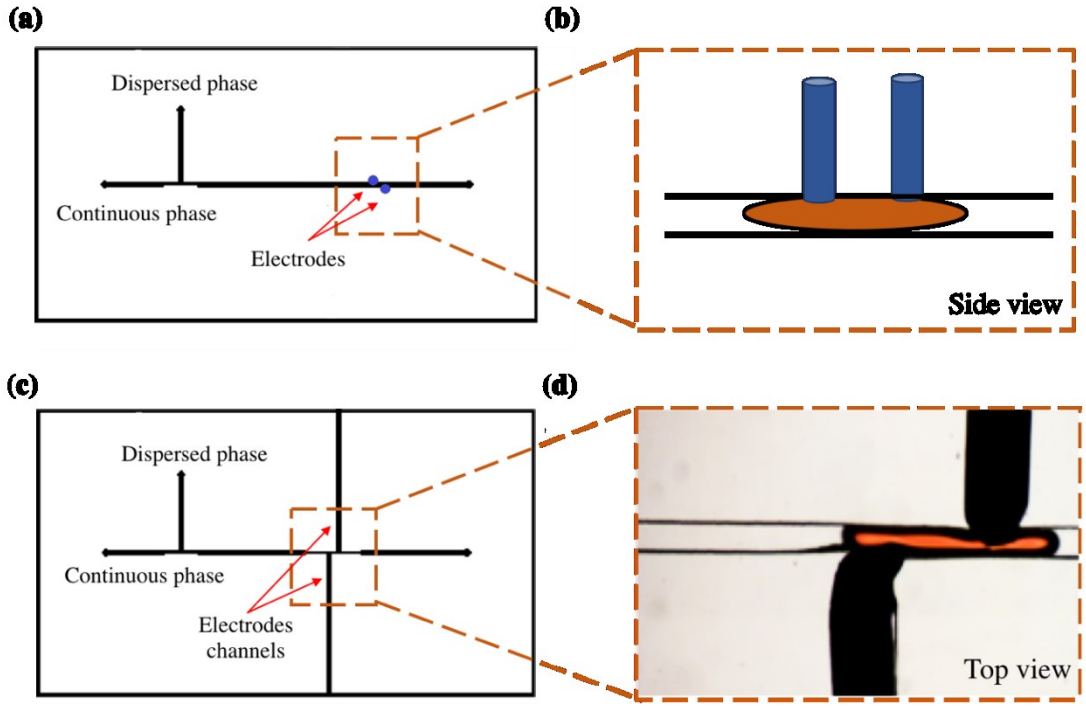

Figure 11: (a) First electrodes design inserted from the top of the main channel, (b) side view of the sleeved electrodes, (c) Second electrodes design where bare Ag wires are inserted from the 200 μm wide side channels, (d) a top view of the second electrodes design

3.2 Results and Discussion

The initial design in figure 11A had some limitations where the sleeved electrodes inserted from the top did not penetrate through the passing droplets on the main channel as illustrated in figure 11B. In this design the surface of the electrodes were coated with oil. Moreover, the empty gaps between the FPE sleeve and the Ag wire acted as an oil trap, preventing the sensing of the droplets by forming a thin film of oil on the tips and the sides of the electrodes. Therefore, this design failed to sense the conductance of the segmented flow.

In the second design as shown in figure 11C the bare electrodes protrude into the passing droplets as in figure 11D. While the second design sensed the initial passing droplets unlike the first design, it had few limitations. The electrodes failed to sense the subsequent flowing droplets due to the multiple oil coatings on the surface of the electrodes from the carrier phase.

The manual insertion of the electrodes from the side channel was challenging. Additionally, the insertion process was mechanically destructive to the PDMS walls causing leakages from the side channels and the baseline of the impedance sensing was unstable. While many challenges had to be addressed in the design presented in figure 11C, it showed the potential of measuring the conductance of the segmented flow.

3.2.1 Electrical Measurement Challenges

3.2.1.1 Leakage

While the side channels for the electrodes' insertion enhanced the sensing of the initial few droplets, special care is needed to prevent the side channel leakage that resulted in disturbances in the segmented flow and the impedance sensing measurements. Due to the size difference between the side channels and the Ag wires, the insertion process widens the side walls of the PDMS resulting in leakage during flow. The leakage was assessed by flowing 1M KCl in the main channel for 5 minutes. In order to improve the sealing of the side channels, drops of incurred PDMS is applied on the sides of both side channels near the outlet of the channels. It is crucial to plasma treat the device before adding the incurred drops of PDMS at 50W for 36s to activate the surfaces of both the glass slide and PDMS to covalently bond with the applied PDMS. Next, the device was left in the oven for the PDMS to solidify. This approach successfully resolved the leakage issue.

3.2.1.2 Baseline

The stability of the baseline is necessary for the consistent, reliable and reproducible segmented flow sensing. In order to test the stability of the baseline, a pressure-driven flow of 1M KCl was maintained for 15-20 minutes in each device. The time required for the baseline

signal to stabilize in newly manufactured devices is tested at different applied voltages. The main resistance in the setup, as measured between the two inserted electrodes, is the device R_{Device}= 5 KΩ measured by a voltmeter as shown in figure 12A, the measurement is consistent with the calculated resistance 5.9 KΩ based on equation 3.3.

$$R = \frac{\ell}{\sigma \times A} \tag{3.3}$$

The initial applied voltage was 312mv in a new fabricated device with freshly chlorinated electrodes. The baseline shows a constant drift before it finally stabilizes as seen in figure 12B. It took 22 minutes to stabilize with an average signal of 5.15 ± 0.06 V with an amplification factor of 10^4 via the transimpedance amplifier, which corresponds to 296 μA. It was hypothesized that some undesired electrochemical effects at the surface of the electrodes was responsible for the observed drift. To minimize these parasitic effects, the voltage bias applied between the two electrodes was reduced to 24 mv to improve baseline stability. In all cases, electrodes were freshly chlorinated for each experiment. The 24 mv value was chosen as it represents the minimum voltage limit of the function generator. Nonetheless, it also caused an initial drift in the baseline as seen in figure 12C and but only took around 3.5 minutes to stabilize. The average registered voltage is 4.67 ± 0.07 V with an amplification factor of 10^5 via the transimpedance amplifier, which corresponds to 30 μA.

A picture of the electrodes is taken with a microscope before and after the baseline was recorded. Figure 12D shows the electrodes before they were exposed to voltage and the electrolyte, and figure 12C after the electrodes been exposed to 312 mv for 20 minutes. The coating on the electrodes surface could be due to the oxidation carried out by the overpotential applied to the circuit. It could also be due to the electrically stimulated redox reaction shown in equation 3.1 and 3.2 causing an initial AgCl deposition on the surface of the electrodes.

According to equation 3.1 and 3.2 when a voltage is applied the same chemical reaction is stimulated in a much higher speed causing the initial instability of the 1 M KCl baseline recording as shown in the states of the electrodes before and after in figure 12.

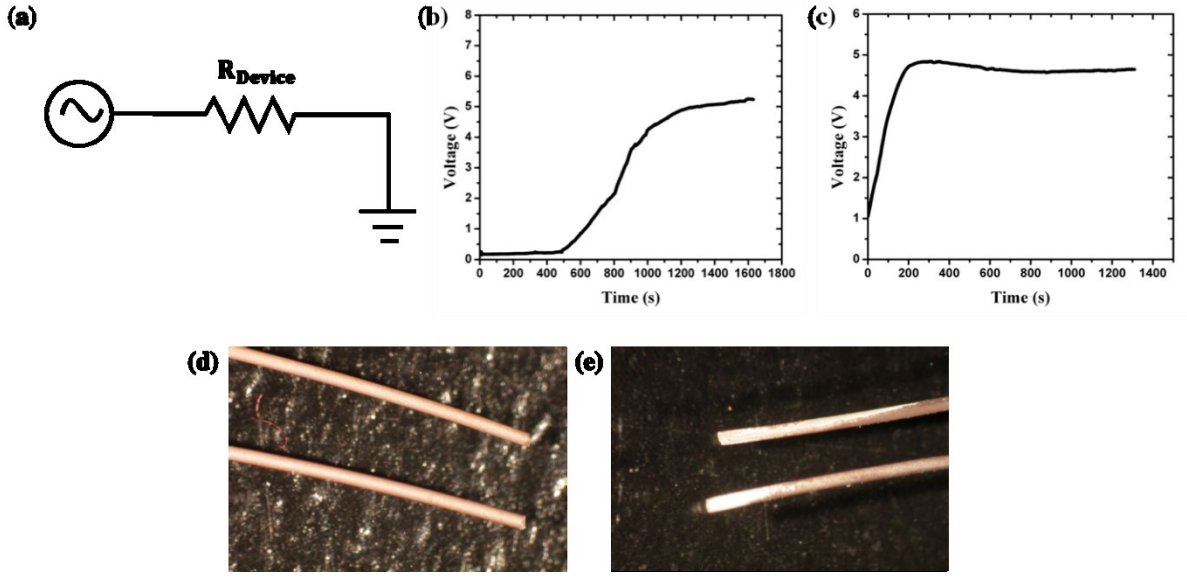

Figure 12: (a) The device is the main resistance in the circuit diagram, (b) the fabricated electrodes behaviour when 312 mv is applied on the system, it shows a long drift in conductance for 22 minutes until it stabilizes, (c) the behaviour of electrodes when 24 mv is applied for conductance measurement, the measurement stabilizes after 3 minutes of exposure, (d) An image of freshly chlorinated 250 μm Ag wires, (e) the 250 μm Ag wires after 20 minutes baseline recording in 1M KCl when 312 mv is applied.

In order to reduce the applied current even further a resistor is added in series with the device to reduce the effect of the overpotential based on Ohms law $V = IR$. The current is reduced to prevent electrodes instability and to resemble the nanopore resistance. The nanopore resistance is approximately 18 MΩ depending on the size of the pore for the future nanopore integration with the droplet microfluidics device.

A 180 KΩ resistance is added to the 5 KΩ device as in figure 13A, therefore the current is reduced which resulted in the reduction of the time required for the baseline stabilization as

seen in figure 13B. By adding the resister, the baseline took 36s to stabilize with an average voltage of 3.56 ± 0.02 V with an amplification factor of 10^7 via the transimpedance amplifier, which corresponds to 0.8 μA. All the measurements are consistent with the expected calculated currents following ohms law.

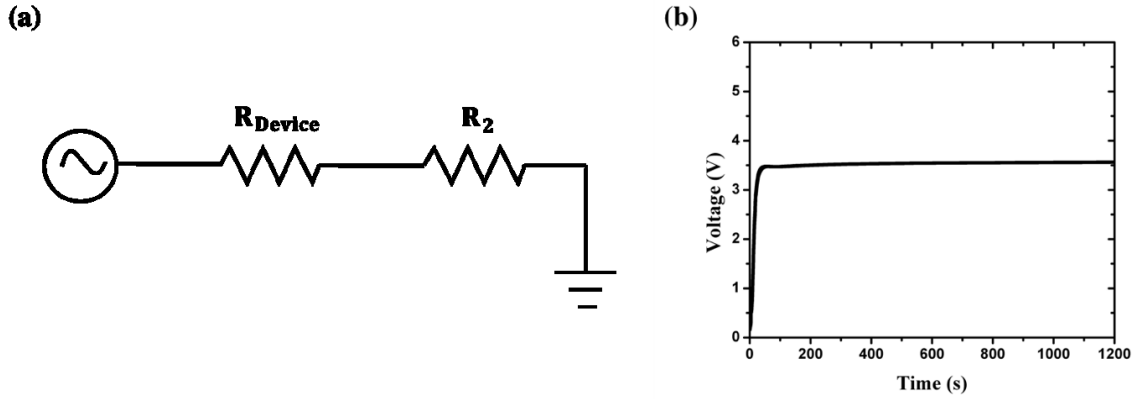

Figure 13: (a) A 180 KΩ resistor is added to the circuit to reduce the current passing through the electrodes, (b) the fabricated electrodes behaviour when 180 KΩ resistor is added, where the baseline stabilizes in 36s.

While increasing the resistance of the system reduces the detection sensitivity, the goal of these sets of experiments is to establish a consistent and reliable sensing of KCl droplets to evaluate the time required for the oil removal from the surface of the electrodes. Additionally, these experiments were needed to test the throughput of the proposed setup in the use of oil as a carrier phase. The sensitivity of the setup will be examined after the integration of nanopore with the use of Axopatch 200B current amplifier instead of the circuit setup shown in figure 10 for single molecules detection.

3.2.1.3 Wettability of the electrodes surface

As expected, the passage of the first few oil segments near the electrodes drops in the measured ionic current to zero. As mentioned earlier the surface of the electrodes is coated by oil preventing further droplets from being sensed or detected by the electrodes as presented in the figure 14B. Various methods were investigated to reduce the hydrophobicity of the electrodes to repel oil or remove it easily from the surface of the electrodes.

The first method used to clean the electrodes was to flow 1M KCL after every oil contact with the electrodes. This achieved the desired results and the subsequent droplets were successfully detected. However, while the rinsing step successfully helped in sensing all droplets effectively, it is time consuming and results in a disruption of the segmented flow regime.

The second approach is plasma treating the electrodes at 50W for 36 s to enhance their wettability. Surface modification by plasma treatment is commonly performed on materials to make them more hydrophilic [65] [66]. As a result, we hypothesized that plasma treating the silver electrodes will reduce their surface hydrophobicity as it does on other materials. The electrodes were plasma treated only once after their insertion in the microfluidics device which was sufficient to increase the hydrophilicity of the electrodes' surface. The goal here is to prevent oil from adhering to the electrodes altogether. The conductance measurement of the segmented flow after the plasma treatment as shown in figure 14C successfully sensed the conductance of droplets. It is observed that electrode wettability lasts for maximum of approximately 10 days in room temperature and 2 days in 70° C oven. However, the device can be plasma treated again if needed to allow longer storage time.

As seen in figure 14D the sensing transition from KCl to oil and vice versa takes around 0.66 ± 0.06 s with a throughput of 0.75 Hz. This approach brings us to a much more reasonable

throughput, especially in the context of nanopore sensing. While fast throughput is needed, the current nanopore sensing technologies needs 5-10 minutes to record enough molecules translocations to significantly differentiate different sample populations. Additionally, the baseline noise increases to 0.5% after the exposure to oil, however, it is assumed to be good enough to proceed with the nanopore integration. Therefore, we predict to face noisy baselines after the nanopore integration due to oil nanodroplets residue on the surface of electrodes and through the nanopore.

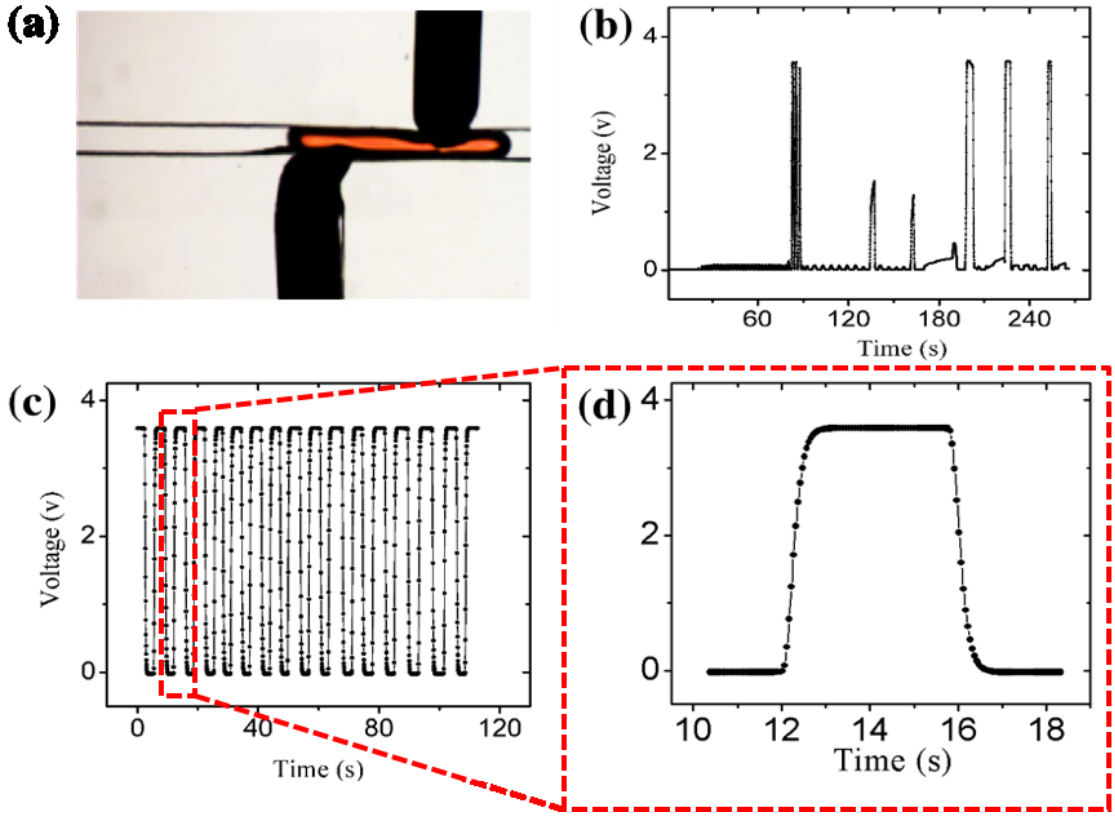

Figure 14: (a) KCl droplet passing by the side electrodes, (b) insensitive conductance sensing of droplets, due to oil contamination on the tip of the electrodes (c) Improved conductance measurement of droplets after the plasma treatment of electrodes (d) conductance of one droplet

Chapter 4 Nanopore Integration and DNA Sensing

This Chapter discusses objective 3 of the project which is the integration of nanopore within the T-junction microfluidics (DMN) device. Solid state nanopore are chosen for the integration within droplet microfluidics, due to their characteristics to sustain the fabrication and device assembly procedures.

The need for synthetic nanopores became a necessity to expand the range of sensing, enhance the durability, and the mechanical and thermal integrity of nanopores. The dielectric materials used for fabricating nanopores are more robust and stable than their biological counterparts [67]. One of the many advantages of artificially made nanopores is the ability to precisely control their size during fabrication, which ranges from approximately 2 nm to tens of nanometers depending on the application [67]. Additionally, they can be integrated within microfluidics, which combines the pre-processing abilities of microfluidics with nanopore sensors [15]. The shape of solid-state nanopores depend on the fabrication method but generally they can be either cylindrical, hourglass-shaped, or resembling a cone [1].

Nanopore membranes are synthesized from a wide range of materials such as silicon nitride, oxides, aluminum-based materials, and graphene [10]. The mechanical properties of silicon-based membranes make them good candidates for solid-state nanopores. Silicon-based membranes are chemically stable, compatible with optical measurement and relatively low stress, which eases the nanopore fabrication process [68]. Furthermore, silicon-based membranes are good insulators and they can withstand a wide range of electrolyte concentrations, temperature and pH [1].

4.1 Solid-state nanopore methods of fabrication

The fabrication process starts from a 100 mm silicon wafer similar to those used in the semiconductor industry, where a typical wafer can produce 200 to 500 chips [18]. The 5mmx5mm silicon chips described in this thesis contain a silicon nitride (SiN_x) membrane with 40 μm x40 μm x12nm dimensions as seen Figure 15A. In figure 15B the two sides of the chip are named to facilitate the explanation of the device fabrication process. Side A corresponds to the T-junction channel where the segmented flow is created, and side B refers to the one straight channel filled with electrolyte.

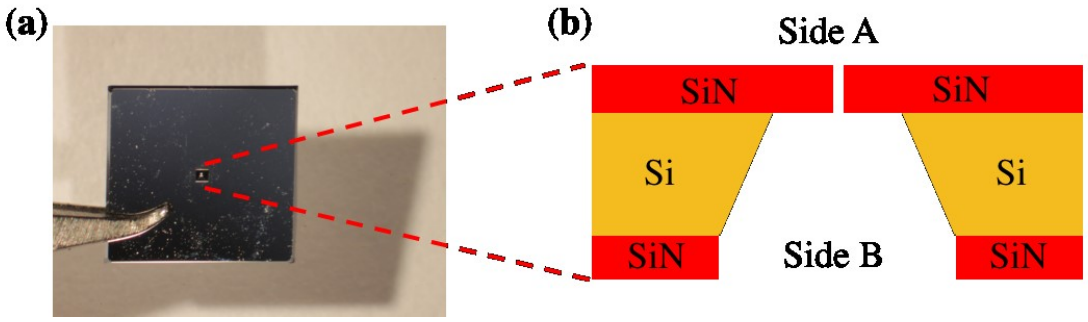

Figure 15: (a) 40x40 SiN membrane in 5mmx5mm silicon chip, (b) schematic of the 40x40 SiN membrane, a Si layer sandwiched between two SiN layers. The two sides of the chip are named to facilitate the explanation of the device fabrication process. Side A corresponds to the segmented flow channel, and side B refers to the one straight channel filled with electrolyte.

There are several ways to sculpt nanopores into thin SiN membranes such as ion and electron bean focusing [69]. The first successful pore sculpting experiment was done in 2001 by focusing an ion beam into a membrane that resulted in a 1.8 nm pore size [69]. The down side of using ion beam fabrication methods is changing the surface charge of the membrane, which can result in unstable pores [69]. Soon after, Storm *et al.* used a transmission electron microscope (TEM) to drill a sub-10 nm hole in a thin silicon nitride membrane [1]. The use of a TEM for nanopore fabrication has been successfully reported in different membrane

materials such as graphene, metal oxides, and silicon nitride [70]. While focused ion beams have been successfully used for nanopore fabrication for almost two decades, the instrumentation required is very expensive and requires highly trained personnel [71]. Therefore, the range of applications that can be targeted by nanopore sensing has been limited and became ultimately restricted to academic settings.

4.1.1 Dielectric Breakdown

In 2014, Kwok *et al.* developed a convenient method of fabrication using controlled dielectric breakdown (CBD) [71]. CBD facilitated the fabrication method, reducing the associated cost, and allowing for the integration within microfluidic devices [66]. CBD nanopores are fabricated by sandwiching a SiN membrane between two reservoirs of 1M KCl electrolyte and applying a high electric field across the intact dielectric membrane, while recording the leakage current [71]. The high electric field ultimately results in a nanopore when a breakdown event occurs [71]. The leakage current is explained as the measurement of the migration of the impurities of the silicon nitride membrane [71]. The attribution of the movement of ions and electrons to the leakage current is neglected, due to the minimal current leakage change in different pH solutions [71]. Moreover, higher leakage current is seen for thicker membranes for the same applied voltage [71]. CBD-fabricated nanopores are initially 2 nm in diameter and can be controllably enlarged to the desired size with nanometer precision [72].

4.1.2 Pore size measurement

The measurement of the nanopore size is continuously performed to stop fabrication, enlarge the pore to the desired size and to constantly check the stability of the pore. Therefore, the theoretical pore size is measured by the experimental open pore conductance value (G).

Conductance is the reciprocal of resistance as illustrated in equation 4.1, where I is the current and V is the applied voltage.

$$G = I/V \tag{4.1}$$

The open pore conductance models assume that the pore is a cylindrical shape and that the voltage drop happens mainly around the nanopore [73]. The G models provide good nanopore conductance estimates when the pore is less than 15 nm in diameter. In this thesis equation 4.2 is used to calculate the circular pore diameter (d), where σ is the bulk conductivity, and l is the membrane thickness [73].

$$G = \sigma\left[\frac{\pi d^2}{4l}\right] \tag{4.2}$$

However, equation 4.2 neglects the effect of access resistance, which dominates in pores larger than 15 nm [74]. Access resistance is the resistance of the electrode/electrolyte interface outside the pore. The access resistance is calculated through the pore diameter and medium conductance as presented in equation 4.3, where ρ is the bulk resistivity and d is the diameter of the pore [73].

$$R_{access} = \frac{\rho}{2d} \tag{4.3}$$

For larger pores Kowalczyk *et al.* model shown in equation 4.4 is used for pore conductance measurement, where access resistance contribution is considered.

In equation 4.4, σ is the bulk conductivity of the electrolyte solution, d is the pore diameter and l is the effective length of the pore, assuming a cylindrical geometry. This model gives a good approximation of pore sizes larger than 15 nm [73].

$$G = \sigma \left[\frac{4l}{\pi d^2} + \frac{1}{d}\right]^{-1} \quad 4.4$$

Both models are geometric, neglecting the surface charge influence due to screening in high salt solutions (typically >1M KCl) [73].

4.2 Background noise in nanopore sensing

The signal to noise ratio is an important factor to consider while sensing. The background noise in nanopores is attributed to flicker noise, thermal noise, dielectric noise, and capacitance noise as shown in figure 16 [75]. Noise is typically displayed in a power spectral density (PSD), which displays the dominant noises in solid-state ionic current measurement based on frequency [80]. PSD plots are the Fourier transformation of the ionic current measurements to a power spectral density plot, where each contributor noise has a specific frequency as shown in figure 16. Flicker noise, which is the dominant source of low frequency noise in solid-state nanopores is seen when a voltage is applied across the membrane, however, the source of flicker noise is not fully understood yet [76]. Thermal noise is independent of the applied voltage and is defined as the thermal fluctuation of a conductive medium caused by the charge carriers [75]. Some of the applied energy across the dielectric membrane is dissipated as heat; the resulting heat and the material loss of the nanopore membrane cause the dielectric noise [75]. The last contributing noise is the capacitance noise from the solid-state chip and electrical circuitry in the setup [75].

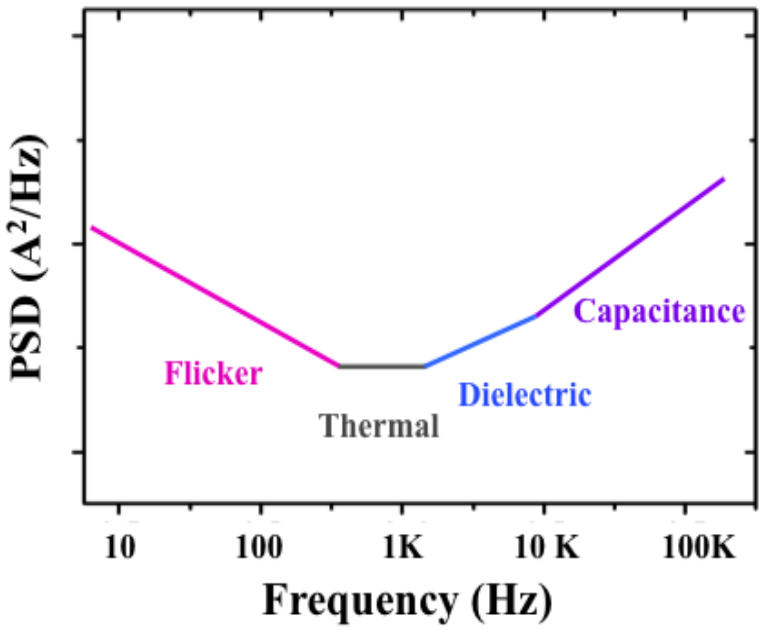

Figure 16: PSD schematic of the dominant noise sources in the ionic current measurement of solid-state nanopore based on frequency, adapted from [75].

4.3 Methods and Results

Figure 17 shows a schematic of the final goal and objective of nanopore-droplet microfluidics integration. As seen in figure 17A when voltage is applied across the nanopore, DNA molecules are detected from the first droplet reaching the sensing area as highlighted in blue in figure 17D. After that the continuous phase (oil) in panel B will drop the current to zero separating the two droplets from cross-talking. Then the second droplet in figure 17C is

directed to the sensing area and DNA molecules are detected as highlighted in blue in D. Figure 17D is a schematic to illustrate the final goal of all the experiments discussed in this chapter.

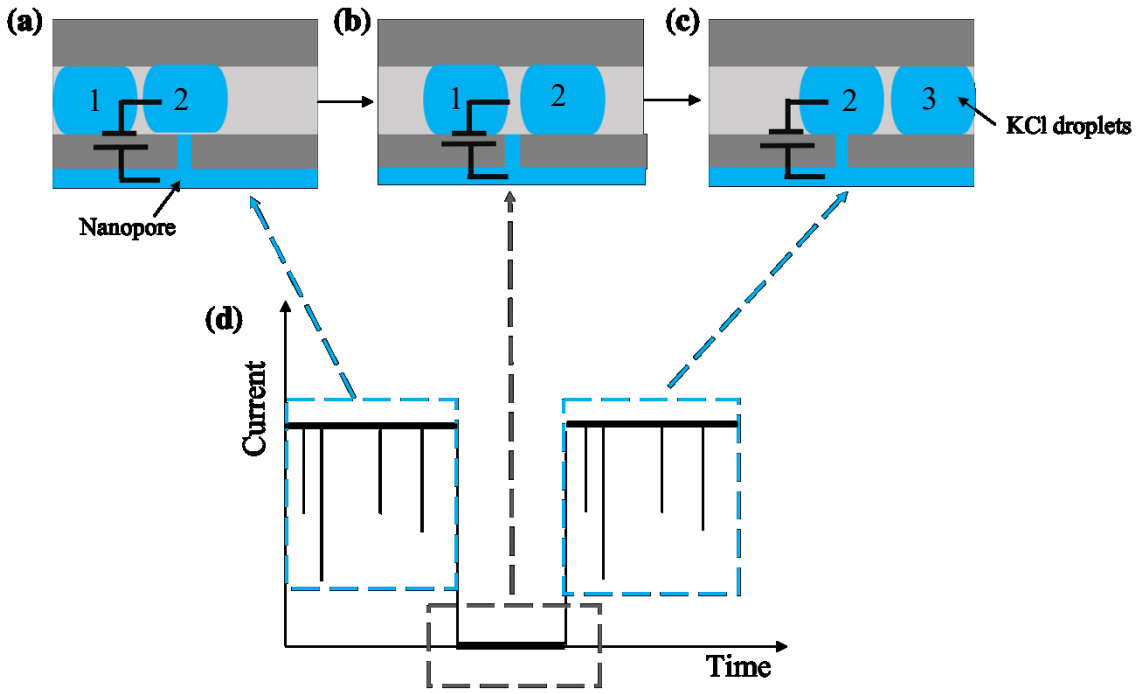

Figure 17: The KCl- oil segmented flow sensing (a) The first directed droplet to the sensing area, (b) the oil separator phase getting to the nanopore, (c) the second droplet sensed by the nanopore sensor, (d) The expected ionic current measurements of the segmented flow, where DNA molecules are sensed from droplets via the nanopore sensor. The blue shows the expected results of droplets sensing, and the grey shows the detection of the oil separator. The graph in d does not show real collected data, rather it is schematics.

The device designed and fabricated in this thesis is a modified derivative from Tahvildari *et al.* integrating nanopore sensors within microfluidic channel arrays [67]. While using the same concept of sandwiching the sensor within two flow channels, this work will incorporate individual droplets detection with a nanopore sensor.

4.4 SiN Chip Integration within Droplet Microfluidics

The schematic of the DMN device sensing area is shown in figure 18, where segmented flow and pure electrolyte surround the nanopore.

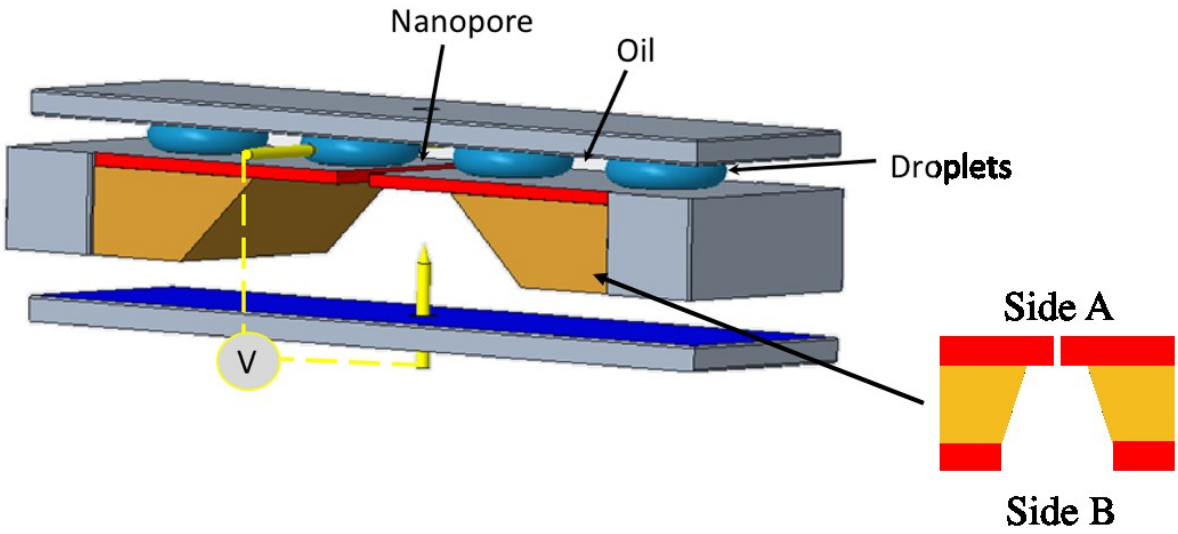

Figure 18: schematic of the DMN device showing the sensing of individual droplets through a nanopore. The fluidic channel below the suspended SiNx membrane is filled with conducting electrolyte.

Various designs were tested in order to achieve successful nanopore sensing of droplets. The first-generation devices contained five PDMS layers, 2 layers added from side A in figure 18 of the SiN chip and 3 layers added from side B shown in figure 18. From side B a flow channel is fabricated with 200 μm width and 80 μm height. Then two 0.75mm in diameter hand punched holes are made through the flow channel for the fluid inlet and outlet, 1.25mm hand punched hole for the AgCl electrode (the same electrode as described in figure 11B) and 3mm hole in the middle of the channel to expose side B of the chip to electrolyte. The flow channel is then bond to a glass slide. Next, the SiN chip is added on top of the 3mm circular hole, then

uncured PDMS is carefully spread around the chip and spin-coated up to 200 μm thickness to compensate for the chip height difference. The compensation layer is exposed for 5-10 minutes to 85° C on a hot plate for the PDMS to partially solidify. Separately fabricated are the two layers which will bind to side A from the chip. 50 μm PDMS height is spin coated on 100x200 μm via wafer, then the T-junction segmented flow layer is bond to the via wafer using a mask aligner to align it in between the two electrodes channels shown in figure 11C. The 100x200x50 μm via size is chosen after testing different sizes of via layers. It was chosen due to the convenient fabrication and better nanopore sensing characteristics. A via layer is a specific shaped hole in a PDMS layer bond to the SiN chip to confine the area exposed to the electrolyte as presented figure 19. Adding a via reduces the exposed area of the chip to electrolyte, thus the applied electrical field that localizes the nanopore creation [6]. Additionally, a via layer reduces the capacitance of the chip by shielding it from the electrolyte, leading to the reduction of the high frequency noise [6]. Subsequently, the two layers of the T-junction and the via layer are bond to side A of the SiN chip. All the layers are plasma treated with 50W, 36s prior to bonding. The device is then placed in a 70° C oven for a minimum of two hours to ensure the complete bonding of the layers. Then, two AgCl electrodes are manually inserted through the two side channels shown in figure 11C. Two electrodes are used from side A to ensure symmetrical electric field lines along with a third electrode from side B to apply a voltage across the SiN membrane for nanopore fabrication.

This design often resulted in trapped bubbles, in the 3mm hole (via) from side B of the chip. The removal of which was mechanically stressful leading to the short lifespan of the nanopore or losing the membrane prior to fabrication.

In the second-generation devices the flow channel from side B is not bind to a glass slide, instead it is bind to 2mm circular via layer with a 100 μm thickness rather than the 3mm depth punch hole.

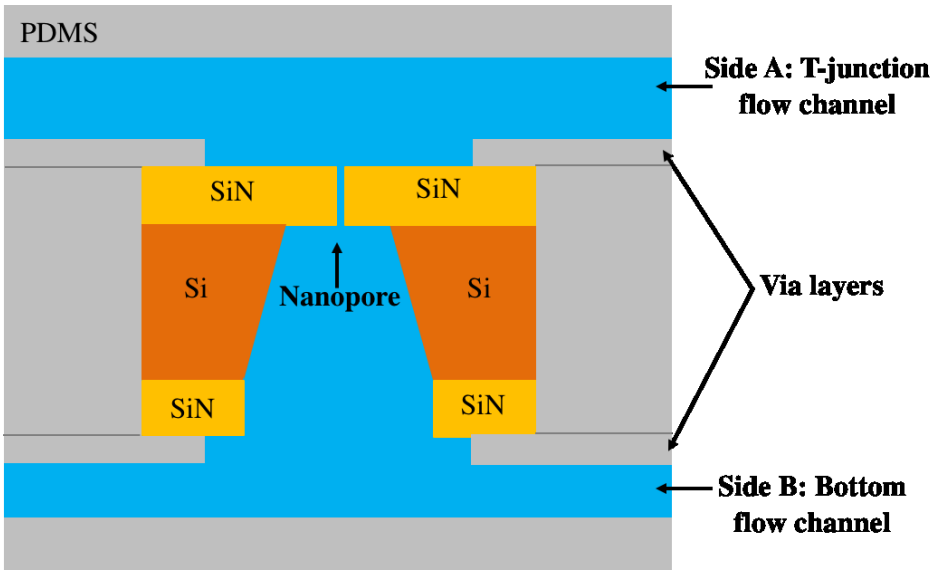

Figure 19: Schematic of the via layers partially covering the SiN chip to localize the applied electric field during nanopore fabrication, all the layers are made from PDMS. (not to scale)

4.4.1 Nanopore Fabrication

Once the device is assembled, nanopore creation is achieved by filling the microchannels (both sides of the insulating SiNx membrane) with 1M KCl electrolyte solutions and applying the proper voltages to the embedded electrodes. The process is controlled by using a customized LabView code. A gradually increasing voltage from 0V to 15V is applied while measuring the leakage current through the membrane as shown in figure 20. When a drastic increase in the current is observed, the applied voltage is stopped, and the conductance is measured to confirm the creation of the nanopore and its size. The initial pore size is typically around 1.5-2.0 nm.

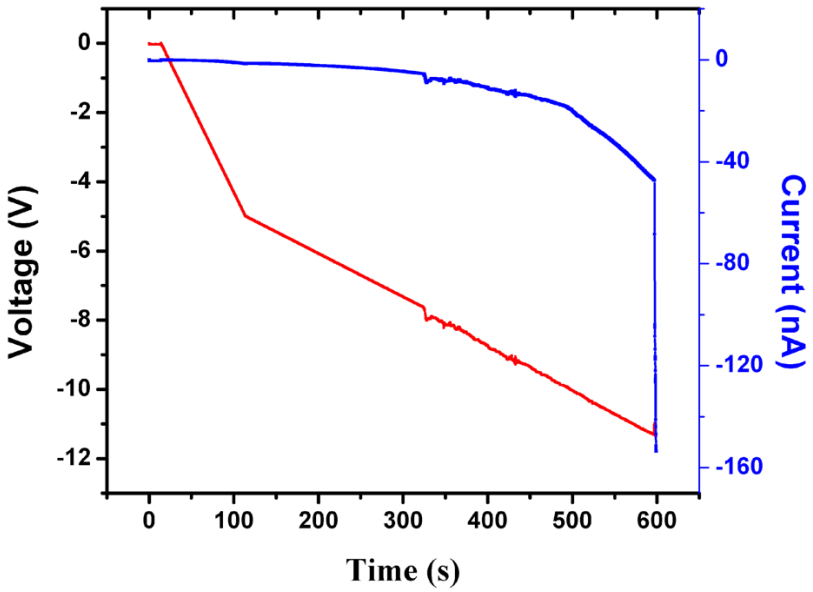

Figure 20: an example of nanopore fabrication on a SiN membrane using CBD method. The leakage current increases proportionally to the applied voltage until a breakdown occurs resulting in the nanopore.

Next, the pore is conditioned by applying alternating +/-3.5V pulses across the membrane to enlarge the pore as seen in figure 21A, while periodically measuring the pore size until the desired size is reached as shown in figure 21B. In addition to enlarging the nanopore, conditioning has been shown to reduce the low frequency noise in the measured ionic current while improving the signal to noise ratio during molecular sensing [6].

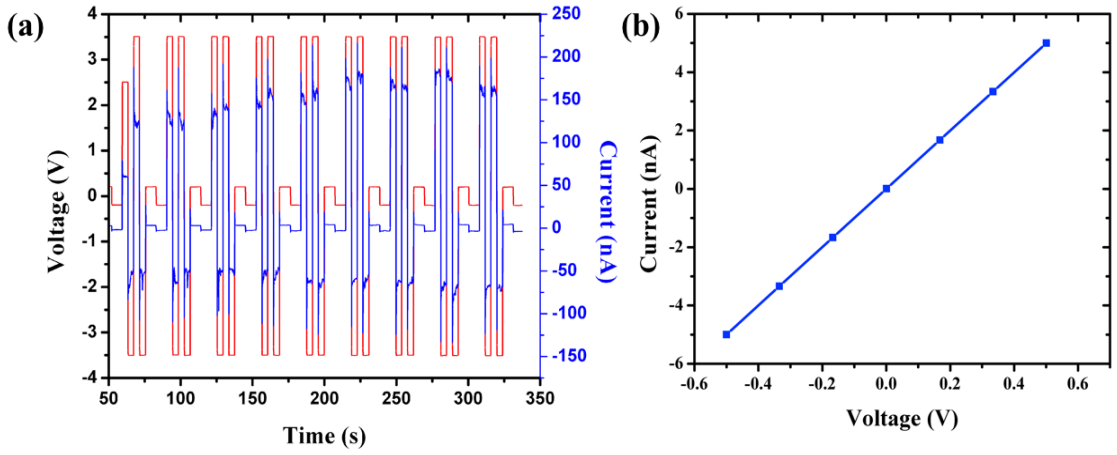

Figure 21: (a) Conditioning of a nanopore by applying +/-3.5V pulses cycles, while measuring the pore size after every cycle, The blue illustrates the open pore current, while the red represents the voltage pulses across a nanopore(b) Current- voltage (I-V) curve for a 5nm pore using a conductance measurement model.

After fabrication, the pore performance is evaluated by measuring the ionic current at a small potential bias (~200mV) and obtaining a power spectral density (PSD) plot to verify electrical noise properties of the nanopore as shown in figure 22. In order to ensure a good sensing environment a power spectral density (PSD) graph is recorded prior and after pore fabrication and in between different experiments. The acquisition of the PSD allows us to properly assess nanopore devices and the noise associated with the measurement signal. The example shown in figure 22 is considered a good device in terms of noise in all frequency ranges, from flicker noise to the capacitance noise. Less than 1K Hz noise indicate flicker noise which can be reduced by ensuring the wettability of the membrane [75]. According to literature nanopore-microfluidics devices a good indicator for a signal to noise PSD registers less than 1 pA^2/Hz between 1K and 100K Hz (dielectric and capacitance noise) [66].

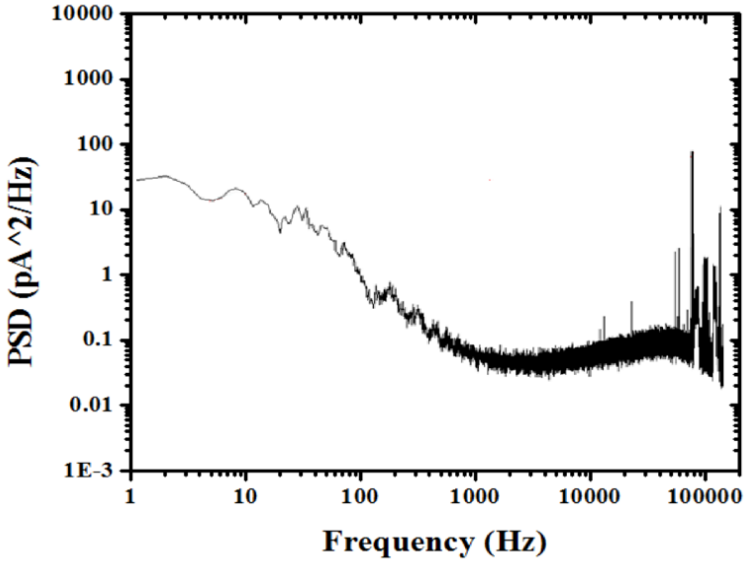

Figure 22: Power spectral density (PSD) noise graph for a 5.9 nm pore size.

4.4.2 Nanopore - Oil Interaction

The second-generation design lead to the continuous clogging of the pore during the initial adjustment of the segmented flow regime. Therefore, oil was introduced to the device as a single continuous flow for 10-15s before introducing KCl as a single flow. This method was followed to study the nanopore-oil interaction since it has not been studied before. As expected, exposure to oil consistently clogged the hydrophilic nanopore. Different strategies were assessed to reverse clogging, as presented in table 6.

Table 6: The investigated strategies to the pore clogging from the segmented flow adjustment

#	Strategies	Results	# Devices tested
1	Pressurizing the flow channel from Side B up to 15 Psi, while maintaining flow in the T-junction channel from side A	Pore remained clogged and the open pore conductance was zero	2
2	Applying a voltage across the membrane up to 15V	Pore remained clogged and the open pore conductance was zero	4
3	Overnight exposure to 1M KCl from both sides of the membrane	The pore partially unclogged	1
4	Flowing 1M KCl on both flow channels for 15-20 minutes while pressurizing the channel from side B	The pore partially unclogged as shown in figure 23, however this solution disturbs the segmented flow	3
5	Flowing Alkaline liquid detergent in side A T-junction channel	The pore unclogged but this solution causes a disturbance in the segmented flow	2
6	Flowing Alkaline liquid detergent in side B flow channel for 1 minute and 1M KCl for 2 minutes	The pore unclogged as seen in figure 24	3
7	Flowing 2% Sodium dodecyl sulphate (SDS) surfactant in side A T-junction channel	The pore unclogged but this solution causes a disturbance in the segmented flow	2
8	Flowing 2% Sodium dodecyl sulphate (SDS) surfactant in side B flow channel	The pore unclogged but kept clogging every few minutes, indicating that oil nanodroplets remained in proximity to the pore	2

While strategies were explored (table 6), we will focus on the two most effective methods to unclog the nanopore after oil exposure. Strategies 1, 2 were not effective, 3 is very time consuming and inefficient, 5 and 8 disturb the segmented flow which can causes cross contamination and constant clogging during the initial droplets' regime formation. Therefore,

strategies 4 and 6 are the most likely to be adapted as a pore cleaning step between droplets' sensing.

Strategy 4 showed the first promising results of clearing the clogged nanopore from oil-nanodroplets. As seen in figure 23A the first 1M KCl droplet shows an open pore conductance of an average of 4600 pA and a calculated pore size of 6.2 nm. Then as expected an oil droplet drops the measurement to zero, a second 1M KCl droplet register an ionic current of zero indicating the nanopore remains clogged. After rinsing with 1M KCl for 15-20 minutes, the nanopore partially unclogs registering an ionic current that corresponds to a nanopore diameter of 2.2 nm. Conditioning the pore afterwards clears the remaining of oil residue in the nanopore, however, testing in 3 different devices conditioning resulted in larger pore sizes. In the device used in figure 23 the final pore size enlarged to 10 nm after conditioning. Figure 23B illustrates that the PSD noise levels after nanopore- oil interaction shows improvement in the thermal and dielectric noise, which could be attributed to oil residue shielding the rest of the membrane, reducing the capacitance of chip. In a recent study painting the sides of the chip with PDMS resulted in lower dielectric and capacitance noise [77]. While PDMS and oil are different, they could both partially coat the insulating membrane and reduce exposure to the electrolyte solution, resulting in lower capacitance noise. Strategy 4 showed the promise of cleaning the nanopore from oil but enlarging the pore after each droplet will result in lower throughput and higher setup complexity.

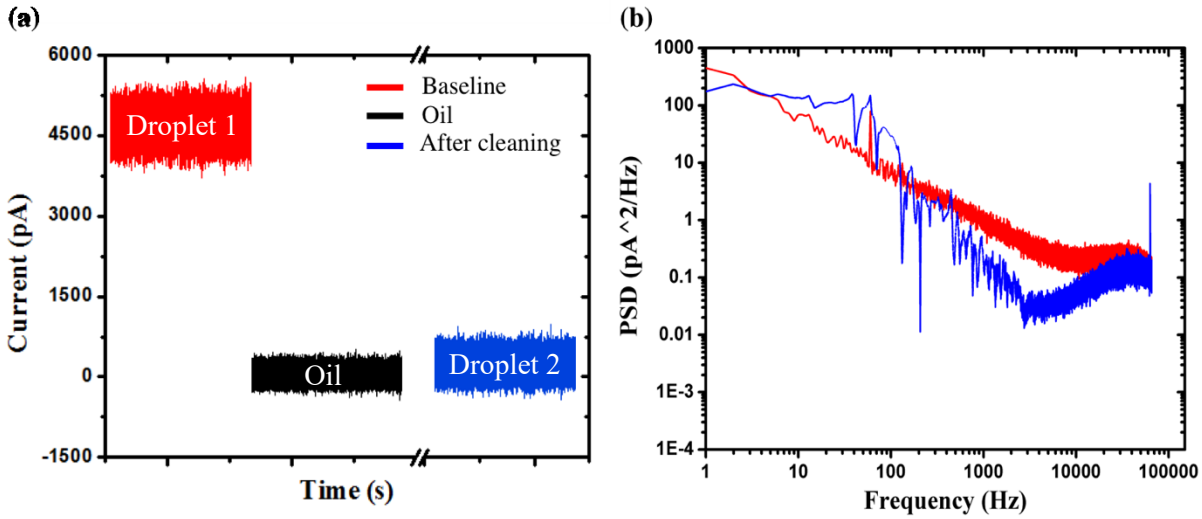

Figure 23: (a) baseline traces before introduction of oil, when oil is introduced, and after rinsing the nanopore from both sides of the membrane for 10-15 minutes. (b) PSD figures illustrating the dominating noise before introduction of oil (red) and after the cleaning step to unclog the pore (blue).

Since strategy 4 successfully cleaned the pore, reducing the time of the cleaning step was the next goal. We hypothesized that since oil is soluble in some detergents, the use of an alkaline detergent might clear and unclog the pore. Therefore, strategy 5 is tested by flowing Alkaline liquid detergent (Contrex ^{TM}) from side A T- junction flow channel, this strategy reduced the cleaning step from 15-20 minutes to 2-3 minutes rinsing time. After that, strategy 6 is implemented which is introducing the same detergent but from side B flow channel instead. The detergent is introduced to the channel for 1 minutes while pressurizing it to drive the detergent through the nanopore, and the introducing 1M KCl for 2 minutes to restore the ionic measurement across the pore. Strategy 6 is developed to prevent the disturbance of the segmented flow regime. In figure 24A traces of the baseline before oil introduction shows a nanopore size of 5.2 nm and after the cleaning step the pore size was 4.3 nm. The pore could be smaller due to either oil residue in the pore or the detergent molecules interaction with the hydrophilic pore, creating a layer of detergent missiles the can result in the reduction of the

pore size. Figure 24B presents the PSD graphs before the introduction of oil and after the cleaning step. The PSD after cleaning the pore with the detergent shows less flicker and thermal noise around the pore which could be from better wetting of the membrane. However, it is more likely to be from the surface charge change resulting from the detergent molecules – nanopore interaction. A recent study reported the coating of SDS detergent of nanopores reduces the noise and enhances DNA and protein molecules detection, resulting in less sticky nanopores, meaning that SDS reduces the interaction of the nanopore walls with the detected molecules [78]. The alkaline detergent used in strategy 6 could have the same effect on the nanopore.

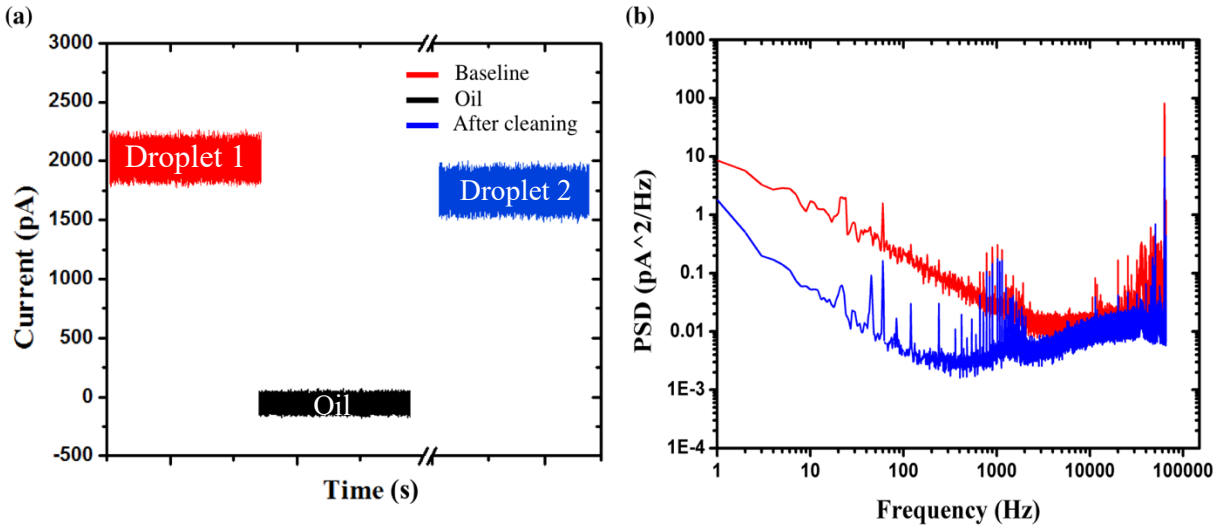

Figure 24: (a) baseline traces before introduction of oil, when oil is introduced, and after rinsing the nanopore from side B of the membrane for 1 minute with an alkaline detergent and 2 minutes of KCl to restore the conductivity for the ionic measurement (b) PSD figures illustrating the dominating noise before introduction of oil and after the cleaning step to unclog the pore. The PSD after the cleaning step shows lower flicker and thermal noise which could be attributed to better wetting of the membrane and surface charge change

Since the alkaline detergent successfully cleared the nanopore in a shorter period of time than the previously presented strategies, SDS is used in strategies 7 and 8 due to its biocompatibility

characteristics. However, the use of 2% SDS as a cleaning detergent in the same way the alkaline detergent was used, resulted in constant clogging of the pore. In other words, the nanopore clogged within minutes of the cleaning steps before introducing any more oil on the nanopore.

The third-generation devices contained microvalves to stabilize the segmented flow regime before sending it to the sensing area. Microvalves consists of two permanently bonded PDMS layers as seen in figure 25A. The rectangular layer is pressurized to deform and block the flow in the rounded flow channel as presented in figure 25B.

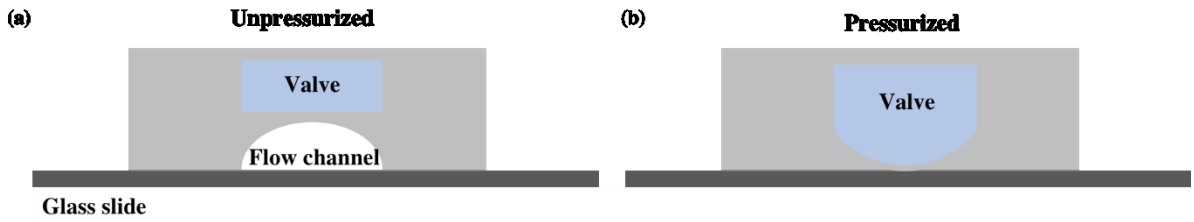

Figure 25: (a) Schematic of a push-down valves above the flow channel. (b) Pressurized pneumatic valve pushes the separating PDMS layer downwards to seal the flow channel. The schematic is adapted from Reference [79] (not to scale)

The pneumatic valves in the third-generation devices were controlled by a customized LabView code (National Instruments) through solenoid valves (SMC S070C-SDG-32) as seen in figure 26A. Solenoid valves are mechanical valves that act as on/off switches.

The microvalves are needed because a nanopore was typically exposed to oil for about 30 seconds during the time required to establish a stable segmented flow. Therefore, the previous experiments were done by introducing a droplet of oil and then 1M KCl to the channel manually to resemble the segmented flow. In segmented flow the nanopore is exposed to the oil carrier phase for 1.14 s on average, while the used method exposed the nanopore to oil for

10-15 s. Therefore, a pneumatic microvalves layer is needed to control the nanopore - oil exposure time. The addition of on-chip microvalves as seen in figure 26A made it possible to prevent oil from clogging the nanopore in these initial moments when segmented flow is stabilized. The nanopore is only exposed to oil once the sample has been successfully compartmentalized into droplets as shown in figure 26A. Looking at figure 26A in the beginning of each experiment prior to the pore creation valve 2 is closed to ensure the ability to establish a stable segment flow. Once the ability to generate a stable segmented flow is confirmed valve 1 is closed for nanopore creation where both flow channels are filled with 1M KCl for the nanopore fabrication and conditioning as explained earlier. After nanopore creation, valve 2 is closed and valve 1 is opened to create a stable segmented flow. The flow rate and droplets' size are adjusted and KCL- oil droplets are collected from outlet 1. Next, valve 1 is slowly closed and valve 2 is opened while the pressure of the dispersed phase is slowly modified simultaneously to maintain the same regime characteristics. The droplets are completely redirected to the sensing area. When the first droplet reaches the nanopore sensor the third valve is pressured to slow down the droplets for sensing. The droplet is immobilized over the nanopore during sensing.

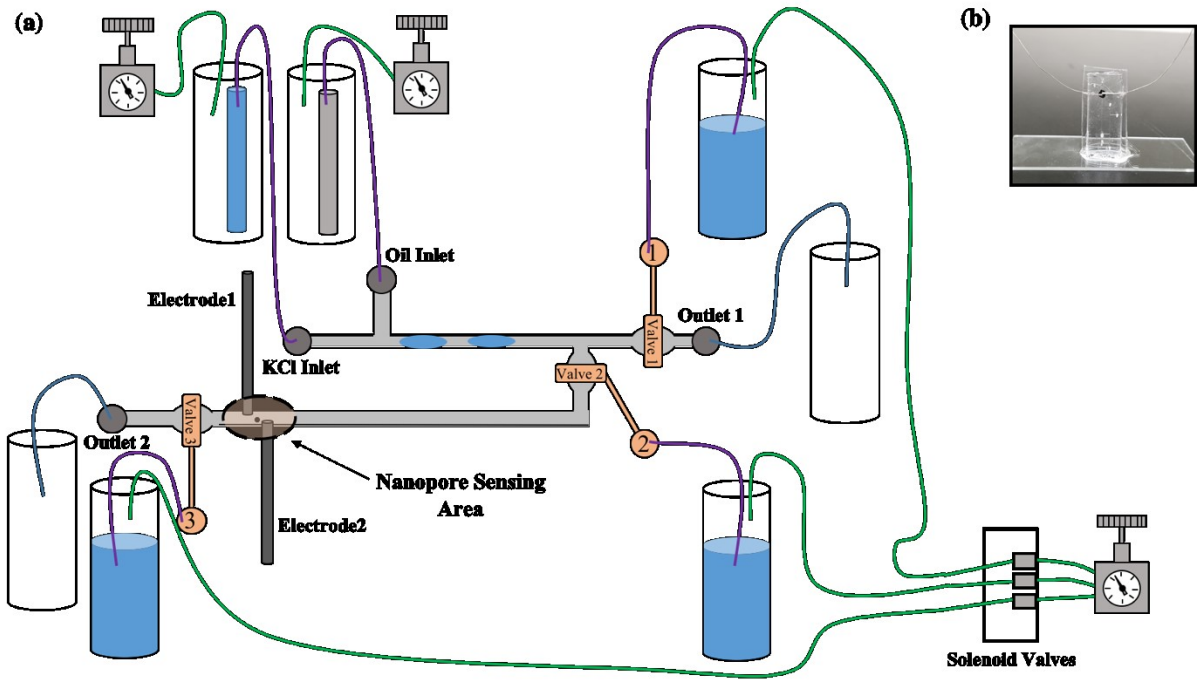

Figure 26: (a) The droplets created by oil and KCl T-junction inlets go through outlet 1 when valve 2 is closed for the segmented flow adjustment and stabilization, then the droplets' size and flow rate is maintained, the flow is slowly redirected to the sensing area containing a nanopore by closing valve 1 and opening valve 2, valve 3 is to slow the droplets' regime for sensing. (b) The DMN device bond to a glass slide horizontally. (not to scale)

The assembly of the third-generation device is similar to what is described in the previous generation devices, in addition to using Az50 X photoresist for the T-junction flow channel to create the rounded edges with a height of 65 μm and 80 μm PDMS spin-coated layer, leaving 15 μm separating membrane between the valves layer and T- junction flow layer. All the layers are bonded by plasma treatment at 50W for 36 s prior. Finally, DMN device is bind to a glass slide by adding few drops of incurred PDMS and exposed to 85° C on a hot plate for 3-5 minutes as seen in figure 26B.

The experimental setup is shown in figure 27A and B, where the DMN device is placed in a shielded copper box (Faraday cage) with all the needed vials to prevent electromagnetic

interference. The nanopore fabrication is performed using a power supply and custom-build circuit shown in figure 27C. The Low-noise electrical measurements are recorded using Axopatch 200B (Molecular Devices) current amplifier. The fabrication leakage current is measured at 10 Hz, while the pore conductance measurements are performed using a sampling rate of 250 kHz and low-pass filter at 100KHz. The segmented flow is stabilized and seen inside the faraday cage by using a mini-microscope, 2x magnification as seen in figure 27D.

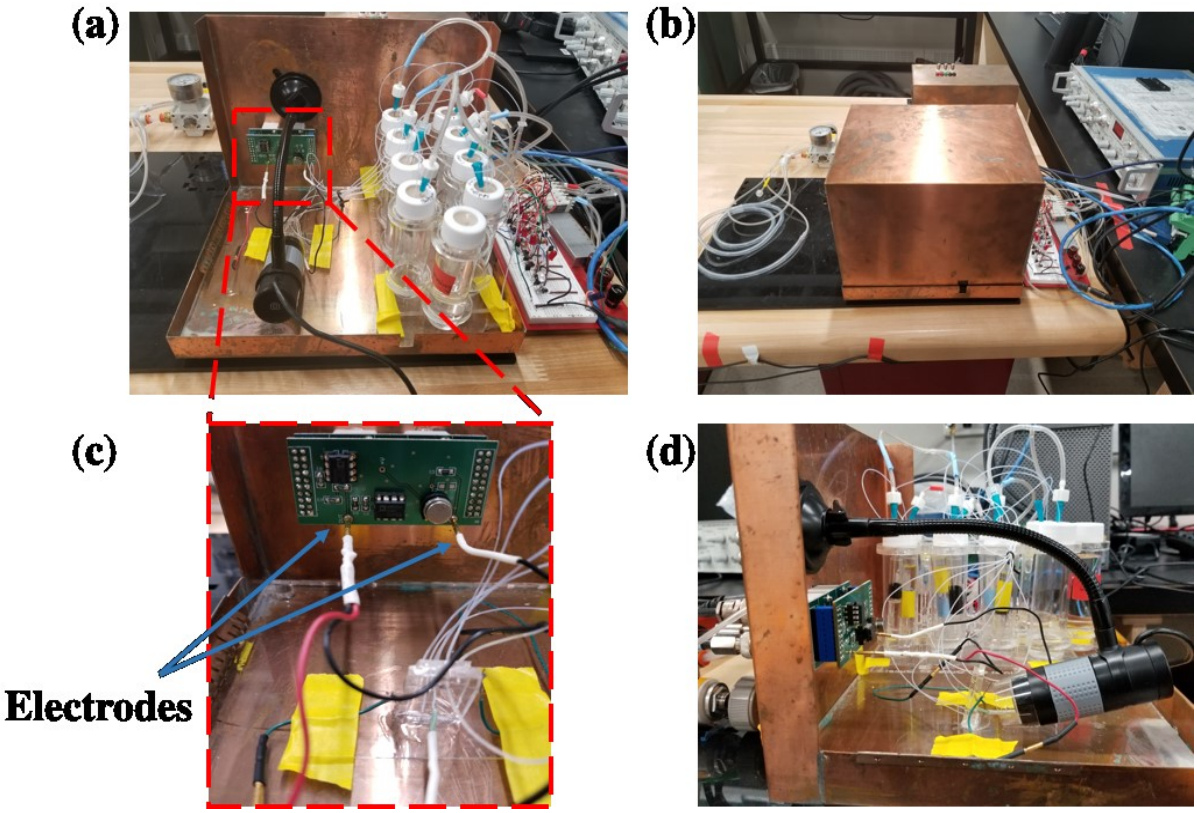

Figure 27: (a) (b) Faraday cage to shield from electromagnetic noise, (c) The built-in circuit used for nanopore fabrication and conditioning, (d) 2x magnification mini-microscope to visualize the stabilization of the segmented flow before measurement.

4.4.3 DNA Sensing

Prior to the segmented flow creation as seen in figure 19, a nanopore is created and benchmarked by running a 1 nM 10kbp dsDNA in 3.6M LiCl (16.3 Sm^{-1}) sample for sensing. DNA is chosen to test the functionality of the nanopore due to its stability and intensive use in nanopore sensors research [1][15]. Based on literature we hypothesize that the different translocation shape and blockage depth seen in figure 28A are due to three possible different molecular translocation conformations of DNA [80][81]. Figure 28B shows when a DNA molecule translocate folded and then in single-file, figure 28C and D show a single DNA molecule translocating single-filed and completely folded, respectively.

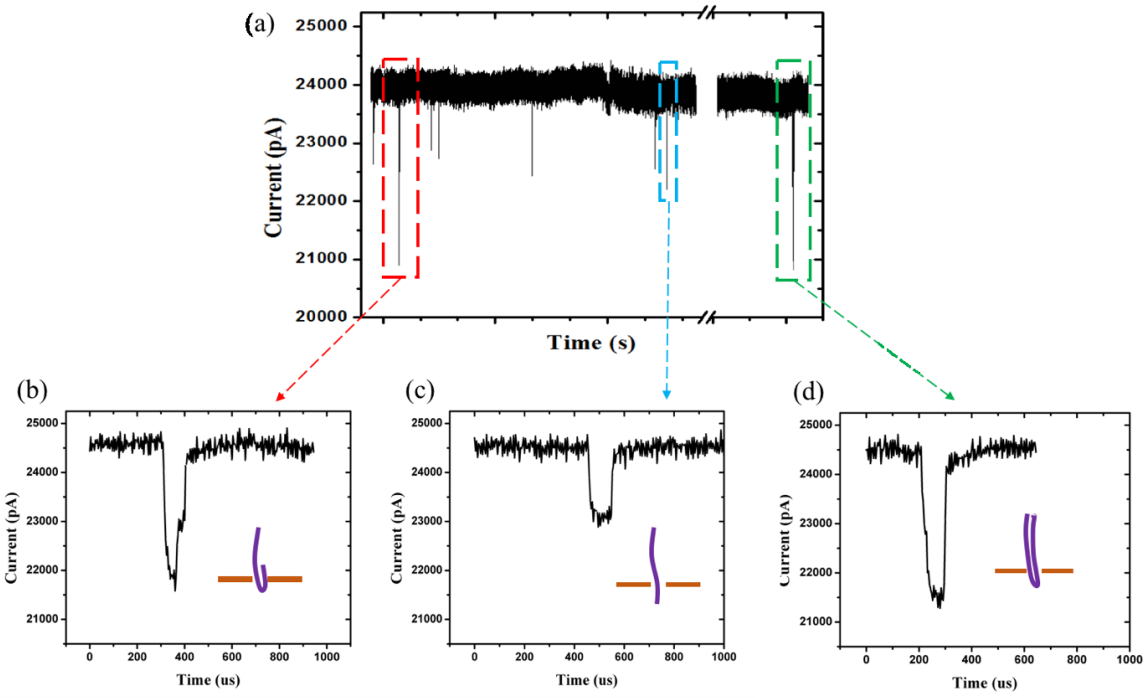

Figure 28: (a) Traces of 10 kbp DNA molecules translocating through a nanopore, (b) a DNA molecule translocating folded initially and then continuing single-filed (c) a DNA molecule translocating single-filed, (d) DNA molecule translocating folded.

The data extracted from these signals are the maximum blockage depth (ΔI) and the dwell time (t_{dwell}). DNA translocation are analyzed by considering the maximum blockage of each translocation, which means extracting the deepest level of blockage in DNA translocation in figure 28A without considering the second single-file level of blockage. The results of the 1 nM 10kbp dsDNA samples translocating in 3.6M LiCl (16.3 Sm^{-1}) through a 16 nm pore is shown in figure 29. The illustrated blockages match the theoretical expected blockages, which are 1058 pA for a single-file and 2117 pA for folded events. While the geometric models give good estimates of the predicted blockages, they treat the nanopore as a cylinder which is not always the case. As expected, the analyzed results show two distinct populations the single-file and the folded events which is approximately double the blockage. The translocation times varies due to DNA- self and pore interaction, it is also believed to be pore size dependent where pores < 5 nm shows lower dwell time distribution [82]

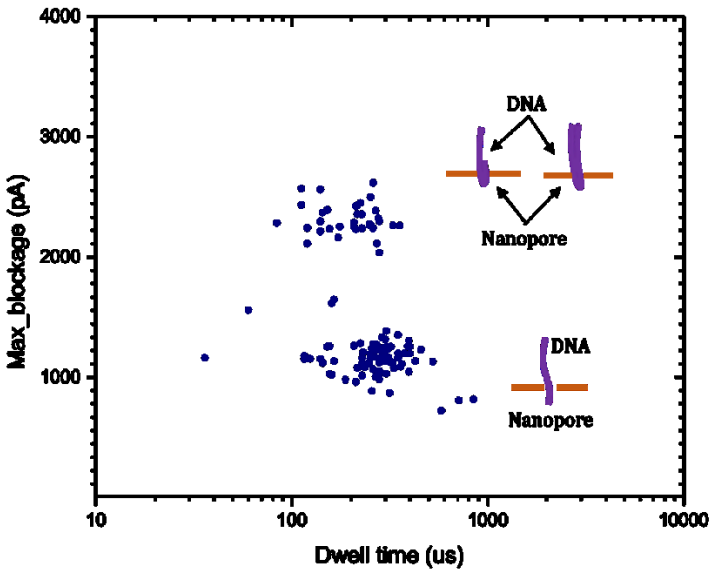

Figure 29: 10kbp 1 nM DNA in 3.6M LiCl sensed through a 16 nm nanopore where two separate populations are observed due to the different conformations of DNA translocation through a nanopore.

After the functionality of the nanopore is validated, we attempted to compartmentalize the sample into individual droplets and detect their DNA content using a nanopore as seen in figure 30.

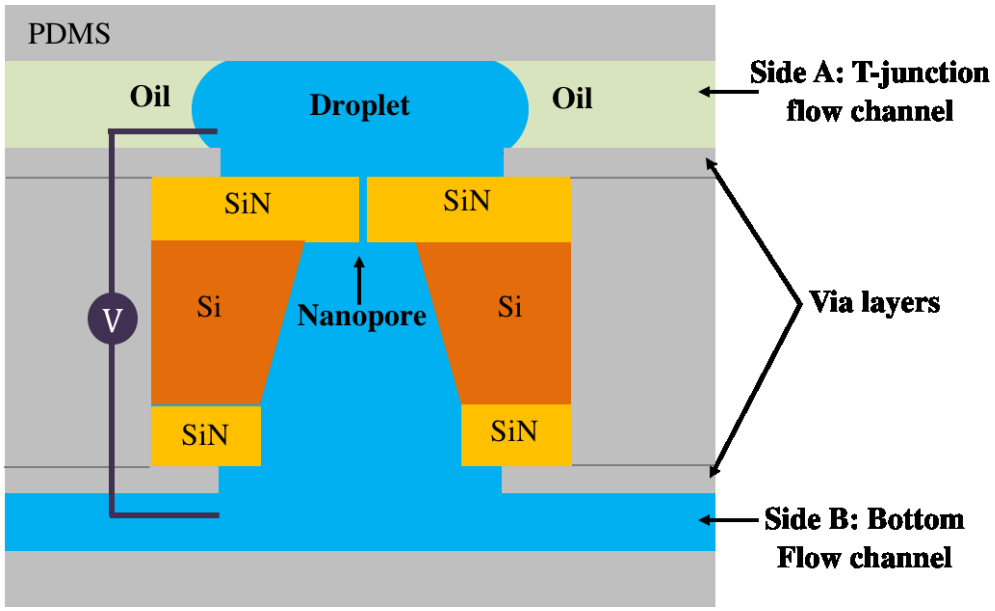

Figure 30: Schematic of the sensing area during a droplet sensing. (not to scale)

The segmented flow is created, stabilized and then send to the sensing area. Figure 31 shows in a different device the sensing of 1M KCl droplets using a nanopore sensor.

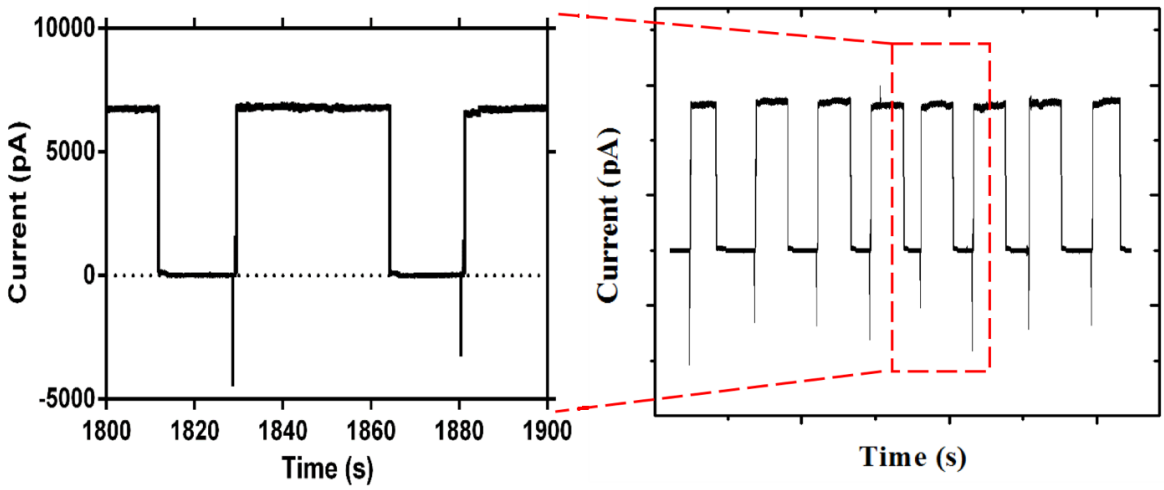

Figure 31: KCl-Oil droplets sensing through a nanopore in DMN device.

We have found that prolonged exposure to the oil separator phase, results in the clogging of a nanopore. Therefore, it is crucial to adjust the droplets regime before sending it to the nanopore sensor. The downward spikes seen in figure 31 shows similar behaviour of a capacitive discharge. Therefore, these spikes could result from the two electrodes in the T-junction flow channel when a droplet touches the first electrode before reaching the nanopore, creating this capacitive discharge.

Next, a DNA sample in an aqueous droplet was sent to the nanopore for sensing, to evaluate the sensing capabilities of the nanopore after oil exposure. The device successfully sensed 10 kbp dsDNA in 3.6M LiCl, as shown in figure 32.

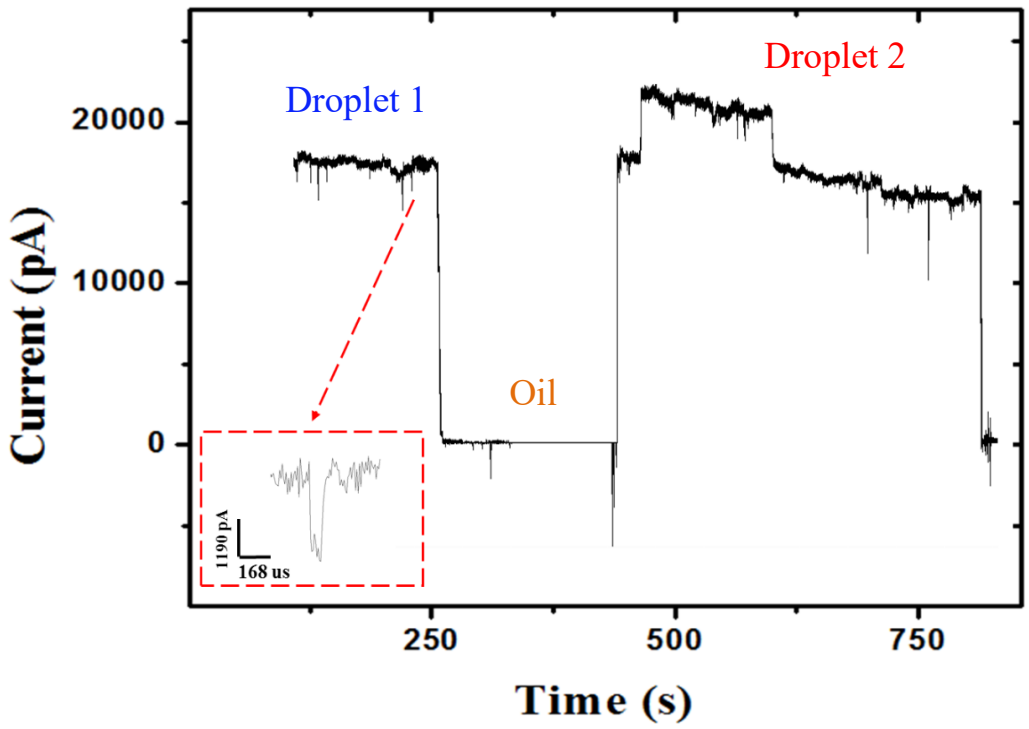

Figure 32: 1 nM 10kbp dsDNA-Oil droplets sensing through a 11 nm nanopore

After the KCl-Oil sensing, the baseline was not as clean as it was previously observed in figure 28 and 31. The DNA population distribution shown in figure 33 are extracted from figure 32 and another sensed droplet. Figure 33A, B, and C show the population distribution of three separate droplets that were interrogated by the nanopore during the same experiment. Figure 33D show the distribution of the three droplets combined. The message behind figure 33 is to show that the blockage depth range of the sensed DNA is consistent throughout droplets sensing which proves the feasibility of sensing DNA within individual droplets using this platform.

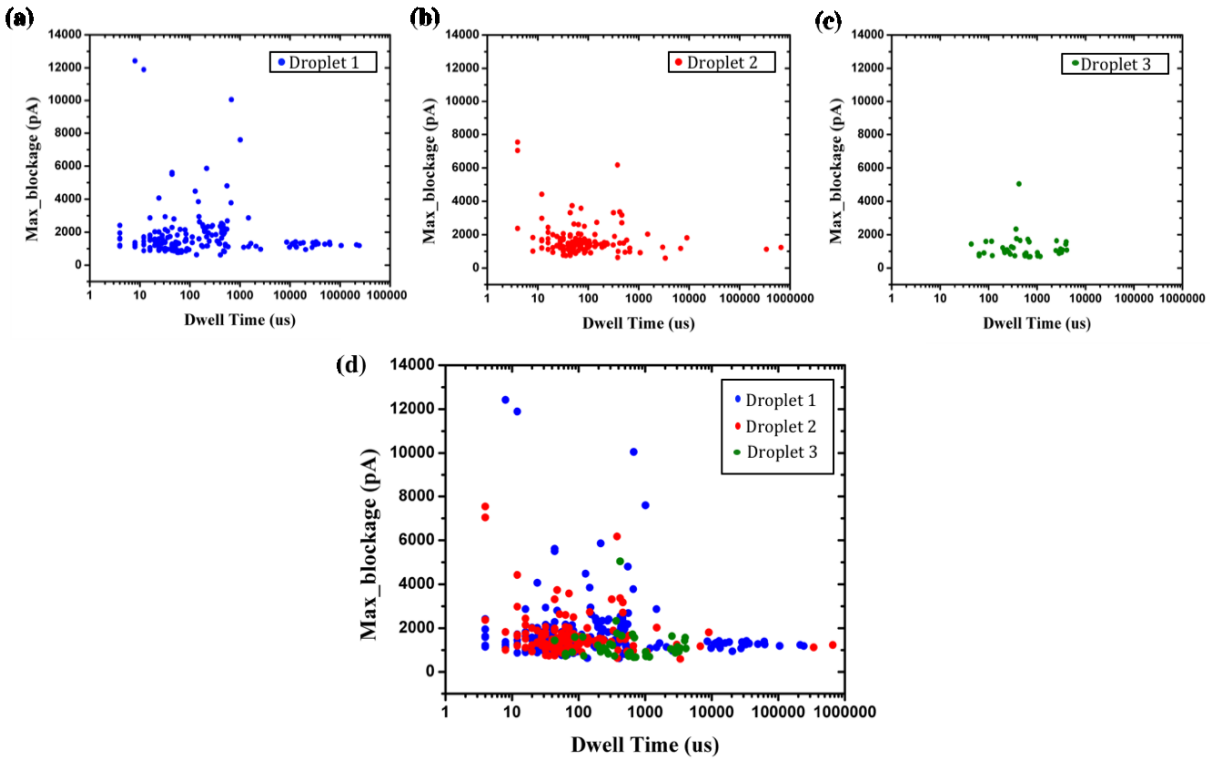

Figure 33: (a) dsDNA translocation distribution in droplet 1, (b) dsDNA translocation distribution in droplet 2, (c) dsDNA translocation distribution in droplet 3, (d) dsDNA translocation distribution for all 3 droplets.

While the DNA populations extracted from sensing within droplets do not show well separated populations as in figure 29, it shows the proof of concept that sensing within droplets is feasible since the pore detected events in the theoretically expected blockages (720 pA) with the signature of translocating DNA molecules as zoomed-in in figure 32. Events less than 40 μs are mostly attributed to hit events, where the DNA register a blockage by interacting with the nanopore without fully translocate through the nanopore. Longer than 1000 μs dwell time events can be explained by DNA-self and nanopore interaction that result in longer

translocation times. Deeper blockages can be the result of multiple molecules trying to translocate at the same time.

4.5 Conclusion

While the DNA translocation within droplets is not ideal, it can be optimized by increasing the sensing time from approximately 6 minutes/ droplet to 10-15 minutes/ droplet to allow more molecules to translocate within a single droplet. Additionally, the baseline within droplets is unstable as seen in figure 32, which could be attributed to the microscopic oil droplets residue on the membrane or a very charged nanopore that increases the DNA-self and nanopore interaction [82]. Additionally, similar noisy baselines have been reported when the nanopore and membrane are not properly wetted [75]. Therefore, oil can act in a similar way to air droplets isolating the nanopore from the electrolyte, causing the unstable and noisy baseline. Furthermore, oil droplets trapped in the nanopore can create partial blockage in the open conductance measurement. Future work in enhancing the baseline signal is needed to improve the sensing capabilities of the nanopore.

Chapter 5 Conclusion and Outlook

There has been increasing interest in integrating nanopore sensors within lab-on-a-chip devices through microfluidics. Nanopore integration in microfluidics previously presented a lot of fabrication challenges due to the use of ion or electron beam fabrication techniques [15]. Controlled dielectric breakdown (CBD) facilitated the integration of solid-state nanopore into microfluidics, which extended nanopore technologies to various types of applications. Nanopore sensors have emerged as a promising technology in detecting single DNA molecules and single nucleotide polymorphism as well as protein unfolding [83]. Droplet microfluidics is a very powerful tool to automate regularly used biological and chemical assays, which will save time and reduce costs. Additionally, it allows the analysis of nano and picolitre volumes of samples, which can be challenging using standard benchtop techniques.

The integration promises exciting new applications of complex fluid manipulation with single molecule sensing abilities [83]. Droplet microfluidics decreases the necessary volumes for samples, the processing time, and increases the efficiency of samples mixing. As demonstrated in the previous chapters of this work, the generation of droplets in the presence of a nanopore sensor was successfully achieved and detected. Moreover, the DNA molecules within those droplets were sensed using the same system.

5.1 Device and Sensing Optimization

As seen this work demonstrates the proof of the feasibility of the concept of integrating a nanopore sensor within droplet microfluidics. However, further work and optimizations have to be done to deliver a higher throughput sensing platform. The major limitation of the current device is the noisy baseline after the nanopore and electrodes are exposed to oil. The noise

could be the cause of the residual oil left in the nanopore or electrodes. The impedance measurement results lead me to believe that noise is not due to the residual oil left on the electrodes. It is more likely that the noise is the cause of the nanopore-oil interaction. A possible noise reduction strategy is combining the current experimental setup with a detergent washing step between droplets sensing which previously shown that it can reduces the baseline noise. However, this has to be further investigated to optimize and reach a stable baseline for single molecule detection.

Minor limitations are related to the complicated fabrication process. Fabricating a microfluidic device with six PDMS layers is vulnerable to various fabrication failures such as valves layer collapsing and leakage issues between the PDMS layers of the device. Valves collapsing is a known issue when using pushdown PDMS pneumatic microvalves, due to the thin PDMS layer separating the valve layer from the flow channel layer as previously demonstrated in figure 25. A way of reducing the leakage problem is by changing the ratio of the polymer and the curing agent of PDMS, then binding the PDMS layers before they are fully cured to improve the adhesion of the layers. Additionally, increasing the height of the PDMS coating on the segmented flow wafer from 80 μm to 90 μm might improve the collapsing issue. The signal to noise ratio can be enhanced by changing the size of the via layers and using PEEK tubes instead of PTFE tubes to reduce the movement of the tubes inside the faraday cage. Furthermore, sensing different types of molecules such as different lengths of DNA and proteins in separate droplets is required to evaluate the sensitivity and specificity of the nanopore in this setup.

5.2 Future Applications

Droplet microfluidics technology is also used in genotyping for disease diagnostics, early intervention of hereditary diseases, and forensics. Currently, the traditional method of analysis is amplifying DNA or RNA samples using PCR, and then analyzing them by using expensive biological and chemical assays [84]. Furthermore, sample preparation of fluids is a necessary step for analysis of complex biological fluids, such as blood and saliva that require lysing, elusion and purification before being analyzed. Droplet microfluidics proposes sample handling, amplification and analysis on the same chip, saving time and cost.

Molecular biology relies heavily on nucleic acid amplification, which is the standard testing tool in all life science fields; it is useful for diagnostics, genetic mutations, and epidemiology [85]. This setup has great promise for various useful and in demand applications.

Single cell encapsulation in droplets while performing LAMP amplification for example is a viable application for the developed DMN device. LAMP doesn't require temperature cycling, which decreases the complexity of the microfluidics setup. As mentioned earlier, LAMP relies on the auto-cycling strand displacement performed by Bst polymerase. Based on equation 1.2, the amplification of DNA produces the precipitate $Mg_2P_2O_7$, which decreases the abundance of ions and nucleotides in the solution resulting in the change of conductance [34]. Therefore, the conductance measured by the AgCl electrodes varies pre and post- amplification, due to the reduction of the number of the charge carriers [86]. The conductance difference and DNA sensing can be detected via the nanopore, to evaluate the success of the amplification if the specific target gene is present in the sample. Additionally, an accurate and high throughput analysis of DNA, RNA and proteins in cancer biology can help improve the understanding of malignant tumors on the cellular and genetic levels. There is a pressing need for new

technologies for cancer biology research, especially for the detection of rare cancer biomarkers, such as circulating tumor cells that exist in very low concentrations in biological samples. A high throughput given the large volume samples is essentially impossible with the currently available technologies [41]. Therefore, breaking the sample into nL range droplets might be the solution for future diagnostic chips.

The DMN device can be altered for food-borne pathogens and agriculture testing. Traditional food borne pathogen testing is implemented by culturing a small sample in an agar plate which is a very time-consuming process [87]

In conclusion, we anticipate that the integration of droplet microfluidics with nanopore sensors will become a powerful tool in DNA, RNA and protein detection as well as in disease diagnosis. However, this technology is still in the early stages of development and needs further work to become a viable alternative to currently available diagnostic tools.

Droplet microfluidics - nanopore diagnosis device offer an alternative for a robust, low cost, and fast diagnostic tools.

References

[1] B. N. Miles, A. P. Ivanov, K. A. Wilson, F. Doğan, D. Japrung, and J. B. Edel, "Single molecule sensing with solid-state nanopores: novel materials, methods, and applications," *Chem Soc Rev*, vol. 42, no. 1, pp. 15–28, 2013.

[2] D. Erickson, S. Mandal, A. H. J. Yang, and B. Cordovez, "Nanobiosensors: optofluidic, electrical and mechanical approaches to biomolecular detection at the nanoscale," *Microfluid. Nanofluidics*, vol. 4, no. 1, pp. 33–52, Jan. 2008.

[3] N. Bhalla, P. Jolly, N. Formisano, and P. Estrela, "Introduction to biosensors," *Essays Biochem.*, vol. 60, no. 1, pp. 1–8, Jun. 2016.

[4] D. Meadows, "Recent developments with biosensing technology and applications in the pharmaceutical industry," *DL Meadows*, vol. 21, no. 3, pp. 179–189, Oct. 1996.

[5] A. Syahir *et al.*, "Label and Label-Free Detection Techniques for Protein Microarrays," *Microarrays*, vol. 4, no. 2, pp. 228–244, Apr. 2015.

[6] B. M. Venkatesan and R. Bashir, "Nanopore sensors for nucleic acid analysis," *Nat Nanotechnol*, vol. 6, no. 10, pp. 615–624, Oct. 2011.

[7] Ralph M. M. Smeets, Ulrich F. Keyser, Diego Krapf, Meng-Yue Wu, and N. H. Dekker, and C. Dekker*, "Salt Dependence of Ion Transport and DNA Translocation through Solid-State Nanopores," 2005.

[8] M. D. Graham, "The Coulter Principle: Foundation of an Industry," *JALA J. Assoc. Lab. Autom.*, vol. 8, no. 6, pp. 72–81, Dec. 2003.

[9] M. D. Graham, "The Coulter principle: Imaginary origins.," *Cytom. A*, vol. 83, no. 12, pp. 1057–61, Dec. 2013.

[10] F. Haque, J. Li, H.-C. Wu, X.-J. Liang, and P. Guo, "Solid-State and Biological Nanopore for Real-Time Sensing of Single Chemical and Sequencing of DNA," *Nano Today*, vol. 812, no. 1, 2013.

[11] R. Austin, "The art of sucking spaghetti," *Nat Mater*, vol. 2, no. 9, pp. 567–568, Sep. 2003.

[12] G. F. Schneider *et al.*, “DNA Translocation through Graphene Nanopores,” *Nano Lett*, vol. 10, no. 8, pp. 3163–3167, Aug. 2010.

[13] A. Oukhaled, L. Bacri, M. Pastoriza-Gallego, J.-M. Betton, and J. Pelta, “Sensing Proteins through Nanopores: Fundamental to Applications,” *ACS Chem Biol*, vol. 7, no. 12, pp. 1935–1949, Dec. 2012.

[14] X. Wang, Y. Li, T. Li, L. Liu, and H.-C. Wu, “The effect of secondary structures on the generation of characteristic events during the translocation of DNA hybrid through α-hemolysin,” *Sci China Chem*, vol. 59, no. 1, pp. 135–141, Jan. 2016.

[15] R. Tahvildari, E. Beamish, V. Tabard-Cossa, and M. Godin, “Lab on a Chip Integrating nanopore sensors within microfluidic channel arrays using controlled breakdown,” vol. 15, 2015.

[16] A. M. Streets and Y. Huang, “Chip in a lab: Microfluidics for next generation life science research.,” *Biomicrofluidics*, vol. 7, no. 1, p. 11302, Jan. 2013.

[17] N. Blow, “Microfluidics: in search of a killer application,” *Nat. Methods*, vol. 4, p. 665, Aug. 2007.

[18] G. M. Whitesides, “The origins and the future of microfluidics,” *Nature*, vol. 442, no. 7101, pp. 368–373, Jul. 2006.

[19] R. Bogue, “MEMS sensors: past, present and future,” *Sens Rev*, vol. 27, no. 1, pp. 7–13, Jan. 2007.

[20] G. M. Whitesides and A. D. Stroock, “Flexible Methods for Microfluidics,” *Phys Today*, vol. 54, no. 6, pp. 42–48, Jun. 2001.

[21] J. C. McDonald *et al.*, “Fabrication of microfluidic systems in poly(dimethylsiloxane).,” *Electrophoresis*, vol. 21, no. 1, pp. 27–40, Jan. 2000.

[22] A. Mata, A. J. Fleischman, and S. Roy, “Characterization of Polydimethylsiloxane (PDMS) Properties for Biomedical Micro/Nanosystems,” *Biomed Microdevices*, vol. 7, no. 4, pp. 281–293, Dec. 2005.

[23] E. Delamarche, A. Bernard, H. Schmid, A. Bietsch, B. Michel, and H. Biebuyck, “Microfluidic Networks for Chemical Patterning of Substrates: Design and Application to Bioassays,” 1998.

[24] C. N. Baroud, F. Gallaire, and R. Dangla, “Dynamics of microfluidic droplets,” *Lab Chip*, vol. 10, no. 16, p. 2032, Aug. 2010.

[25] B. ROTMAN, “Measurement of activity of single molecules of beta-D-galactosidase.,” *Proc Natl Acad Sci U A*, vol. 47, pp. 1981–91, Dec. 1961.

[26] S.-Y. Teh, R. Lin, L.-H. Hung, and A. P. Lee, “Droplet microfluidics,” *Lab Chip*, vol. 8, no. 2, p. 198, Jan. 2008.

[27] M. R. Neuman, *The Biomedical Engineering Handbook: Second Edition*. CRC Press LLC, 2000.

[28] B. Vogelstein and K. W. Kinzler, “Digital PCR,” *Proc. Natl. Acad. Sci.*, vol. 96, no. 16, pp. 9236–9241, Aug. 1999.

[29] S. L. Spurgeon, R. C. Jones, and R. Ramakrishnan, “High Throughput Gene Expression Measurement with Real Time PCR in a Microfluidic Dynamic Array,” *PLoS One*, vol. 3, no. 2, p. e1662, Feb. 2008.

[30] J. Bell, “The polymerase chain reaction,” *Immunol Today*, vol. 10, no. 10, pp. 351–355, Oct. 1989.

[31] *Advanced Topics in Forensic DNA Typing: Methodology*. Elsevier, 2012.

[32] T. Notomi *et al.*, “Loop-mediated isothermal amplification of DNA,” *Nucleic Acids Res*, vol. 28, no. 12, p. 63, 2000.

[33] Y. Mori, K. Nagamine, N. Tomita, and T. Notomi, “Detection of loop-mediated isothermal amplification reaction by turbidity derived from magnesium pyrophosphate formation.,” *Biochem Biophys Res Commun*, vol. 289, no. 1, pp. 150–154, Nov. 2001.

[34] X. Zhang *et al.*, “Quantitative determination of target gene with electrical sensor,” *Sci Rep*, vol. 5, no. 1, p. 12539, Dec. 2015.

[35] P. Garstecki, A. M. Gañán-Calvo, and G. M. Whitesides, “Formation of bubbles and droplets in microfluidic systems,” *Bull Pol. Acad Sci Tech Sci*, vol. 53, no. 4, 2005.

[36] A. G€ Unther and M. T. Kreutzer, “Multiphase Flow,” *Micro Process Eng*, vol. 1.

[37] W.-L. Chou, P.-Y. Lee, C.-L. Yang, W.-Y. Huang, and Y.-S. Lin, “Recent Advances in Applications of Droplet Microfluidics,” *Micromachines*, vol. 6, no. 9, pp. 1249–1271, Sep. 2015.

[38] O. J. Dressler, R. M. Maceiczyk, S.-I. Chang, and A. J. DeMello, “Droplet-Based Microfluidics,” *J Biomol Screen*, vol. 19, no. 4, pp. 483–496, Apr. 2014.

[39] I. G. Lignos, R. C. R. Wootton, A. J. DeMello, and B. M. Stone, “Segmented Flow Microfluidics,” in *Encycl. Biophys.*, Berlin, Heidelberg: Springer Berlin Heidelberg, 2013, pp. 2300–2306.

[40] J. Chen *et al.*, “Assembly-line manipulation of droplets in microfluidic platform for fluorescence encoding and simultaneous multiplexed DNA detection.,” *Talanta*, vol. 134, pp. 271–277, Mar. 2015.

[41] D.-K. Kang, M. Monsur Ali, K. Zhang, E. J. Pone, and W. Zhao, “Droplet microfluidics for single-molecule and single-cell analysis in cancer research, diagnosis and therapy,” *TrAC Trends Anal Chem*, vol. 58, pp. 145–153, Jun. 2014.

[42] J.-W. Choi, G.-J. Kim, S. Lee, J. Kim, A. J. DeMello, and S.-I. Chang, “A droplet-based fluorescence polarization immunoassay (dFPIA) platform for rapid and quantitative analysis of biomarkers,” *Biosens Bioelectron*, vol. 67, pp. 497–502, May 2015.

[43] Y. Piao, D. J. Han, M. R. Azad, M. Park, and T. S. Seo, “Enzyme incorporated microfluidic device for in-situ glucose detection in water-in-air microdroplets,” *Biosens Bioelectron*, vol. 65, pp. 220–225, Mar. 2015.

[44] J. Lankelma, Z. Nie, E. Carrilho, and G. M. Whitesides, “Paper-Based Analytical Device for Electrochemical Flow-Injection Analysis of Glucose in Urine,” *Anal. Chem.*, vol. 84, no. 9, pp. 4147–4152, May 2012.

[45] P. Wägli, Y.-C. Chang, A. Homsy, L. Hvozdara, H. P. Herzig, and N. F. de Rooij, “Microfluidic Droplet-Based Liquid–Liquid Extraction and On-Chip IR Spectroscopy Detection of Cocaine in Human Saliva,” *Anal. Chem.*, vol. 85, no. 15, pp. 7558–7565, Aug. 2013.

[46] R. Prakash, K. Pabbaraju, S. Wong, A. Wong, R. Tellier, and K. V. I. S. Kaler, “Droplet Microfluidic Chip Based Nucleic Acid Amplification and Real-Time Detection of Influenza Viruses,” *J Electrochem Soc*, vol. 161, no. 2, pp. B3083–B3093, Dec. 2013.

[47] T. S. Kaminski, O. Scheler, and P. Garstecki, “Droplet microfluidics for microbiology: techniques, applications and challenges,” *Lab. Chip*, vol. 16, no. 12, pp. 2168–2187, 2016.

[48] H. Gu, M. H. G. Duits, and F. Mugele, “Droplets Formation and Merging in Two-Phase Flow Microfluidics,” *Int. J. Mol. Sci.*, vol. 12, no. 4, pp. 2572–2597, Apr. 2011.

[49] J. H. Xu, A. S. W. Li, A. J. Tan, and A. G. S. Luo, “Correlations of droplet formation in T-junction microfluidic devices: from squeezing to dripping.”

[50] A. Günther and K. F. Jensen, “Multiphase microfluidics: from flow characteristics to chemical and materials synthesis,” *Lab. Chip*, vol. 6, no. 12, pp. 1487–1503, Nov. 2006.

[51] R. Seemann, M. Brinkmann, T. Pfohl, and S. Herminghaus, “Droplet based microfluidics,” *Rep Prog Phys*, vol. 75, pp. 16601–41, 2012.

[52] J. K. Nunes, S. S. H. Tsai, J. Wan, and H. A. Stone, “Dripping and jetting in microfluidic multiphase flows applied to particle and fiber synthesis.,” *J Phys Appl Phys*, vol. 46, no. 11, Mar. 2013.

[53] A. S. Utada, A. Fernandez-Nieves, H. A. Stone, and D. A. Weitz, “Dripping to Jetting Transitions in Coflowing Liquid Streams,” *Phys Rev Lett*, vol. 99, no. 9, p. 094502, Aug. 2007.

[54] “Transition from squeezing to dripping in a microfluidic T-shaped junction,” *J Fluid Mech*, vol. 595, pp. 141–162, 2008.

[55] X.-B. Li, F.-C. Li, J.-C. Yang, H. Kinoshita, M. Oishi, and M. Oshima, “Study on the mechanism of droplet formation in T-junction microchannel,” *Chem. Eng. Sci.*, vol. 69, no. 1, pp. 340–351, Feb. 2012.

[56] C. A. Stan, S. K. Y. Tang, and G. M. Whitesides, “Independent Control of Drop Size and Velocity in Microfluidic Flow-Focusing Generators Using Variable Temperature and Flow Rate,” *Anal. Chem.*, vol. 81, no. 6, pp. 2399–2402, Mar. 2009.

[57] Hsien-Yeh Chen, and Y. Elkasabi, and J. Lahann*, “Surface Modification of Confined Microgeometries via Vapor-Deposited Polymer Coatings,” 2005.

[58] F. Allhoff, P. Lin, and D. Moore, *What is nanotechnology and why does it matter? : from science to ethics*. Wiley- Blackwell, 2010.

[59] A. Del Campo and C. Greiner, "SU-8: a photoresist for high-aspect-ratio and 3D submicron lithography," *J Micromech Microeng*, vol. 17, pp. 81–95, 2007.

[60] W. B. Glendinning and J. N. Helbert, *Handbook of VLSI microlithography : principles, technology, and applications*. Noyes Publications, 1991.

[61] L. F. Thompson and R. E. Kerwin, "POLYMER RESIST SYSTEMS FOR PHOTO- AND ELECTRON LITHOGRAPHY."

[62] W. H. Teh, U. Dürig, U. Drechsler, C. G. Smith, and H.-J. Güntherodt, "Effect of low numerical-aperture femtosecond two-photon absorption on (SU-8) resist for ultrahigh-aspect-ratio microstereolithography," *J Appl Phys*, vol. 97, no. 5, p. 054907, Mar. 2005.

[63] D. Ives, *Reference electrodes, theory and practice,*. New York: Academic Press, 1961.

[64] G. J. Janz and D. J. G. Ives, "Silver, Silver Chloride Electrodes," *Ann. N. Y. Acad. Sci.*, vol. 148, no. 1, pp. 210–221, Feb. 1968.

[65] P. K. Chu, J. Y. Chen, L. P. Wang, and N. Huang, "Plasma-surface modification of biomaterials," p. 64, 2002.

[66] R. Tahvildari *et al.*, "Manipulating Electrical and Fluidic Access in Integrated Nanopore-Microfluidic Arrays Using Microvalves," p. 1602601, 2016.

[67] F. Xiao *et al.*, "Fabrication of massive sheets of single layer patterned arrays using lipid directed reengineered phi29 motor dodecamer.," *ACS Nano*, vol. 3, no. 1, pp. 100–7, Jan. 2009.

[68] A. J. Storm, J. H. Chen, X. S. Ling, H. W. Zandbergen, and C. Dekker, "Fabrication of solid-state nanopores with single-nanometre precision," *Nat Mater*, vol. 2, no. 8, pp. 537–540, Aug. 2003.

[69] J. Li, D. Stein, C. McMullan, D. Branton, M. J. Aziz, and J. A. Golovchenko, "Ion-beam sculpting at nanometre length scales," *Nature*, vol. 412, no. 6843, pp. 166–169, Jul. 2001.

[70] M. D. Fischbein and M. Drndić, "Electron beam nanosculpting of suspended graphene sheets," *Appl Phys Lett*, vol. 93, no. 11, p. 113107, Sep. 2008.

[71] H. Kwok, K. Briggs, and V. Tabard-Cossa, "Nanopore Fabrication by Controlled Dielectric Breakdown," *PLoS One*, vol. 9, no. 3, p. e92880, Mar. 2014.

[72] E. Beamish, H. Kwok, V. Tabard-Cossa, and M. Godin, "Fine-tuning the Size and Minimizing the Noise of Solid-state Nanopores," *J Vis Exp*, no. 80, pp. e51081–e51081, Oct. 2013.

[73] S. W. Kowalczyk, A. Y. Grosberg, Y. Rabin, and C. Dekker, "Modeling the conductance and DNA blockade of solid-state nanopores," *IOP Publ Nanotechnol Nanotechnol*, vol. 22, pp. 315101–5, 2011.

[74] I. Vodyanoy and S. M. Bezrukov, "Sizing of an ion pore by access resistance measurements.," *Biophys J*, vol. 62, no. 1, pp. 10–1, Apr. 1992.

[75] V. Tabard-Cossa, "Instrumentation for Low-Noise High-Bandwidth Nanopore Recording," *Eng Nanopores Bioanal Appl*, pp. 59–93, Jan. 2013.

[76] C. Danelon, C. Santschi, J. Brugger, and H. Vogel, "Fabrication and Functionalization of Nanochannels by Electron-Beam-Induced Silicon Oxide Deposition," *Langmuir*, vol. 22, no. 25, pp. 10711–10715, Dec. 2006.

[77] V. Tabard-Cossa, D. Trivedi, M. Wiggin, N. N. Jetha, and A. Marziali, "Noise analysis and reduction in solid-state nanopores," *Nanotechnology*, vol. 18, no. 30, p. 305505, 2007.

[78] D. Müter, T. Shin, B. Demé, P. Fratzl, O. Paris, and G. H. Findenegg, "Surfactant Self-Assembly in Cylindrical Silica Nanopores," *J. Phys. Chem. Lett.*, vol. 1, no. 9, pp. 1442–1446, May 2010.

[79] Kwang W Oh and Chong H Ahn, "A review of microvalves," *J. Micromechanics Microengineering*, vol. 16, no. 5, p. R13, 2006.

[80] M. Wanunu, J. Sutin, B. McNally, A. Chow, and A. Meller, "DNA Translocation Governed by Interactions with Solid-State Nanopores," *Biophys. J.*, vol. 95, no. 10, pp. 4716–4725, Nov. 2008.

[81] F. Nicoli, D. Verschueren, M. Klein, C. Dekker, and M. P. Jonsson, "DNA Translocations through Solid-State Plasmonic Nanopores," *Nano Lett.*, vol. 14, no. 12, pp. 6917–6925, 2014.

[82] S. Carson, J. Wilson, A. Aksimentiev, and M. Wanunu, “Smooth DNA Transport through a Narrowed Pore Geometry,” *Biophys. J.*, vol. 107, no. 10, pp. 2381–2393, Nov. 2014.

[83] T. Jain, R. Jose, S. Guerrero, C. A. Aguilar, and R. Karnik, “Integration of Solid-State Nanopores in Microfluidic Networks via Transfer Printing of Suspended Membranes,” 2013.

[84] J. V. Pagaduan, V. Sahore, and A. T. Woolley, “Applications of microfluidics and microchip electrophoresis for potential clinical biomarker analysis.,” *Anal. Bioanal. Chem.*, vol. 407, no. 23, pp. 6911–6922, Sep. 2015.

[85] K. B. Mullis, “The unusual origin of the polymerase chain reaction.,” *Sci Am*, vol. 262, no. 4, pp. 56–61, 64–5, Apr. 1990.

[86] M.-J. Tang *et al.*, “Rapid and Sensitive Detection of Listeria monocytogenes by Loop-Mediated Isothermal Amplification,” *Curr Microbiol*, vol. 63, no. 6, pp. 511–516, Dec. 2011.

[87] S. Neethirajan, I. Kobayashi, M. Nakajima, D. Wu, S. Nandagopal, and F. Lin, “Microfluidics for food, agriculture and biosystems industries.,” *Lab. Chip*, vol. 11, no. 9, pp. 1574–1586, May 2011.

[88] J. Hill *et al.*, “Loop-mediated isothermal amplification assay for rapid detection of common strains of Escherichia coli.,” *J Clin Microbiol*, vol. 46, no. 8, pp. 2800–4, Aug. 2008.

[89] C. Ma *et al.*, “A novel method to control carryover contamination in isothermal nucleic acid amplification,” *Chem Commun*, vol. 53, no. 77, pp. 10696–10699, 2017.

Appendix

LAMP Preliminary Results

Preliminary experiments were done using the WarmStart® LAMP amplification kit (BioLabs). The LAMP amplification was done on MalB DNA using six different primers adapted from the Hill *et al* study shown in table 7 [88]. The reaction mixture contained 12.5 μL of 2x master mix, 0.5 μL CYBER green fluorescent dye, 1.6 μM of FIP and BIP, 0.2 μM of F3 and B3, 0.4 μM loopF and loopB and DI water to reach 25 μL final volume. The negative and positive samples were incubated for an hour at 65º C in a qPCR thermocycler to initiate the amplification reaction.

Table 7: MalB gene LAMP primers

Primer	Sequence
F3	GCC ATC TCC TGA TGA CGC
B3	ATT TAC CGC AGC CAG ACG
BIP	CTG GGG CGA GGT CGT GGT ATT CCG ACA AAC ACC ACG AAT T
FIP	CAT TTT GCA GCT GTA CGC TCG CAG CCC ATC ATG AAT GTT GCT
LOOP F	CTT TGT AAC AAC CTG TCA TCG ACA
LOOP B	ATC AAT CTC GAT ATC CAT GAA GGT G

A gel electrophoresis was run to evaluate the success of the LAMP amplification shown in figure 33.

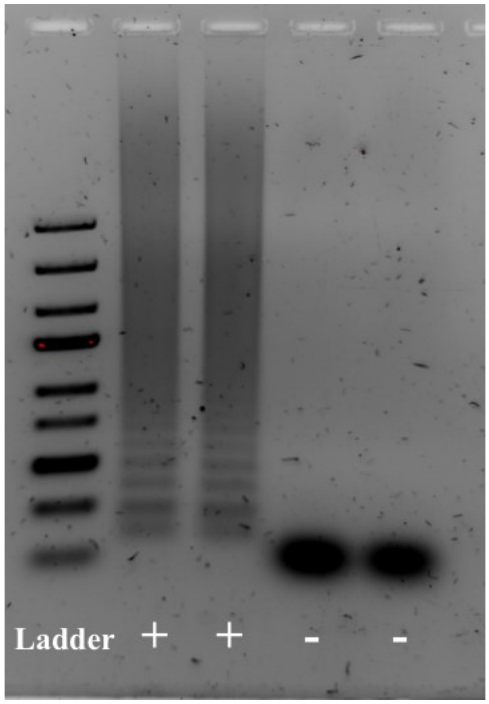

Figure 34: Gel electrophoresis image to check the success of the LAMP amplification, (+) is the positive sample that has the MalB gene, (-) is the negative control without the MalB gene

The positive (has the MalB gene) and negative (without the MalB gene) samples were tested using droplets microfluidics. The conductivity was measured with the AgCl side electrodes prior to the integration of nanopore. The results were inconclusive due to the lower sensitivity of the measurement setup. X. Zhang *et al.* demonstrated a 0.68% conductance difference between the positive sample (with the target gene) and negative samples (same mixture without the target gene) from 1.478V to 1.468V [34]. Future work for this application requires increasing the sensitivity of the conductance measurement due to the small difference of the conductance change. Increasing the sensitivity of the sensing setup can be implemented by measuring the conductance via a nanopore sensor using the current amplifier (Axopatch 200B). Additionally, LAMP amplification is highly sensitive to contamination and false

positives [89]. Therefore, confining the LAMP reaction within droplets in a lab on a chip device can reduce the risk of cross contamination.

Device Evolution

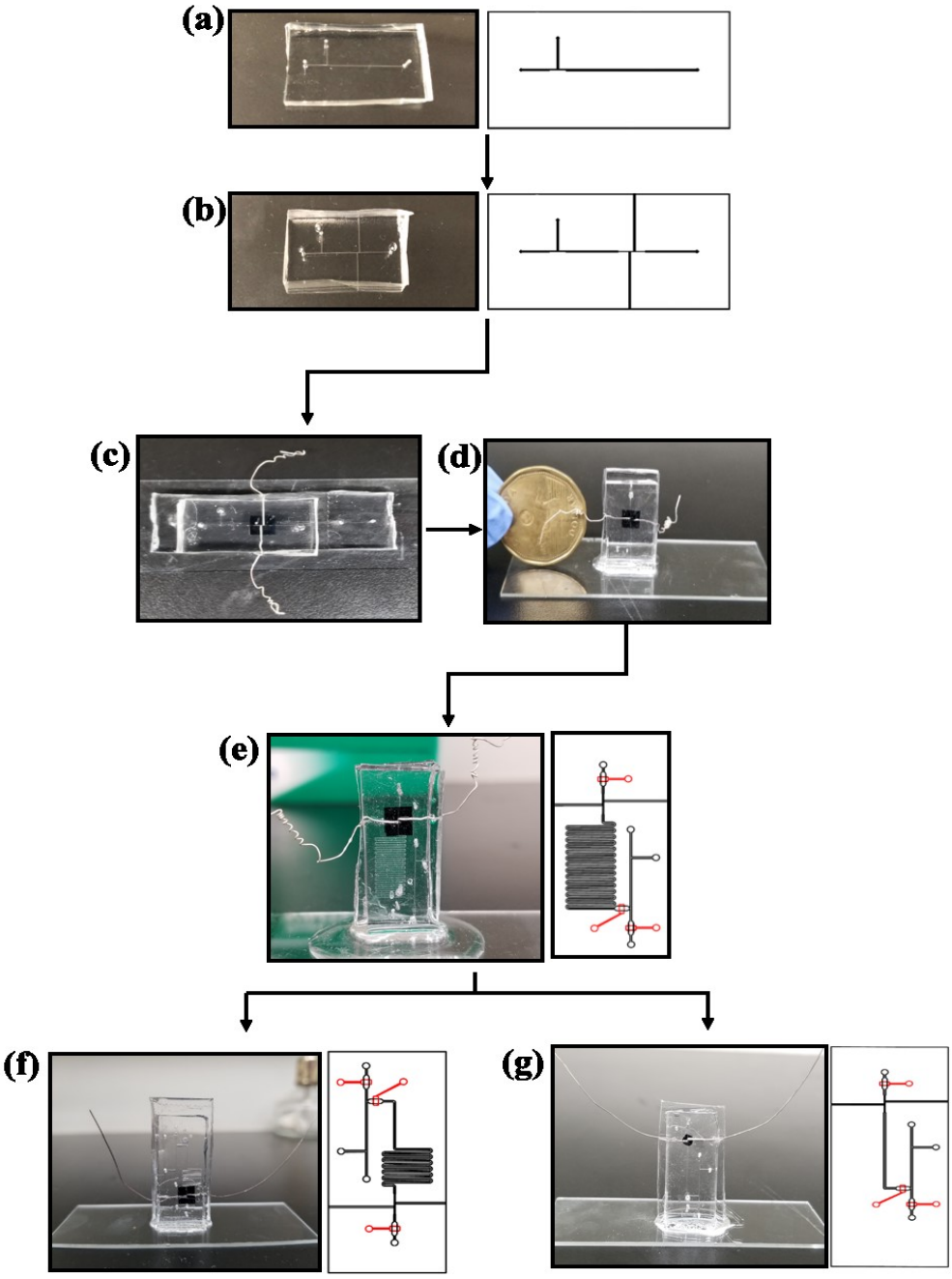

Figure 35: Device evolution, (a) T-Junction design for droplets formation, (b) AgCl electrodes side channels design for conductance sensing, (c) first generation of the Silicon Nitrite chips integration within microfluidics, (d) second generation of DMN device for droplet sensing via the nanopore sensor, (e) Third generation to integrate the valves layer to stabilize the droplets regime before sending it to the nanopore region, (f) and (g) due to the high channel resistance of (e) the serpentine was reduced or eliminated.